Taphonomic bias on calcareous micro and nannofossils and paleoenvironmental evolution across the Messinian Salinity Crisis onset:
Insights from the Sorbas Basin (SE Spain).

(Article begins on next page)

27 February 2025

1 **Taphonomic bias on calcareous micro and nannofossils and paleoenvironmental**

2 **evolution across the Messinian Salinity Crisis onset: insights from the Sorbas Basin (SE**

3 **Spain)**

4 Mancini[a], A. M., Gennari[a], R., Natalicchio[a], M., Dela Pierre[a], F., Carnevale[a], G., Pastero[a], L., Pellegrino[a], L.,

5 Pilade[a], F., Lozar[a], F.

6 [a] Dipartimento di Scienze della Terra, Università degli Studi di Torino, Via Valperga Caluso 35, 10125 Torino, Italy.

7 Corresponding author: alanmaria.mancini@unito.it

8 **Abstract**

9 During the Messinian Salinity Crisis (MSC, 5.97-5.33 Ma) the synergy between tectonic and climatic

10 processes promoted the deposition of evaporites throughout the Mediterranean Basin. The

11 disappearance of calcareous nannofossils and foraminifers at the MSC onset has been traditionally

12 interpreted as the result of the establishment of hypersaline conditions in the water column, which

13 were lethal for most marine eukaryotes. Here, we investigate the calcareous micro and nannofossil

14 assemblages from the Sorbas Basin (SE Spain) spanning the onset and the first phase of the MSC (~

15 5.9-5.7 Ma) in order to test whether their disappearance was related to adverse environmental

16 conditions and/or to preferential dissolution of biogenic calcite. Micropaleontological analyses and

17 petrographic observations suggest that the disappearance of calcareous fossils was the result of a

18 taphonomic bias related to paleoceanographic changes that favoured the oxidation of both pyrite and

19 organic matter at the sea floor. A poorly preserved benthic and planktic assemblage and aragonitic

20 laminated sediment characterize the deposits of the first phase of the MSC from 5.93 Ma onward;

21 aragonite deposition was likely bio-mediated in response to enhanced photosynthesis, as suggested by

22 its $\delta^{13}C$ signature. The fossil assemblage preserved in these deposits indicates a shallowing upward

23 trend of the basin with respect to the pre-evaporitic phase, and the establishment of a lagoon-like

24 environment characterized by episodic improvement of the connections with the open sea. We

25 conclude that the temporary disappearance of calcareous fossils approximately at the MSC onset was

26 related to ongoing basin restriction, which increased the sensitivity of the basin to fresh-water input

27 and temperature changes, promoting marked fluctuations of the redox conditions in bottom sediments.

28 This finding challenges the view of a marine biotic crisis related to hypersaline conditions at the MSC

29 onset and opens new perspectives on the paleoenvironmental conditions that characterized this time

30 interval.

31 ## 1- Introduction

32 The Messinian Salinity Crisis (MSC) is commonly regarded as the most extreme event that affected

33 the Mediterranean region during its recent geological history (e.g. Hsü et al., 1977). This event was

34 promoted by the tectonically-driven restriction of the connection between the Mediterranean Basin and

35   the Atlantic Ocean (Flecker et al., 2015; Capella et al., 2018; Corbí et al., 2020), eventually leading to

36   widespread evaporite deposition in the marginal and deep Mediterranean basins. Such a restriction

37   proceeded by steps (Kouwenhoven et al., 1999; Vasiliev et al., 2019; Kontakiotis et al., 2019; Corbí et

38   al., 2020; Zachariasse et al., 2021; Kontakiotis et al., 2022), as indicated by the sedimentary and fossil

39   records (Kouwenhouven et al., 2006; Mancini et al., 2020). These restriction steps decreased both the

40   water exchange between the Mediterranean and the Atlantic Ocean and the bottom water circulation in

41   the Mediterranean Basin (Kouwenhouven et al., 1999; Bulian et al., 2022). The last step preluding the

42   onset of the crisis is marked by the recently described MSC onset bioevent (5.99 Ma; Lozar et al., 2018;

43   Lozar and Negri, 2019; Mancini et al., 2020), consisting of a succession of peaks of abundance of

44   certain calcareous nannofossil (CN) taxa, such as *Sphenolithus abies*, followed or accompanied by

45   abundance peaks of *Helicosphaera carteri*, *Umbilicosphaera rotula* and *Rhabdosphaera clavigera*

46   (Lozar et al., 2018; Gennari et al., 2018; Lozar and Negri, 2019). According to Mancini et al. (2020),

47   this event was probably triggered by the restriction of the Mediterranean basin which became more

48   sensitive to continental freshwater input.

49   During the MSC, increased seawater salinity was thought to be responsible for both gypsum and

50   halite deposition and for the establishment of a biotic crisis, with consequent gradual diversity decline

51   and final disappearance of most marine eukaryotes (Blanc-Valleron et al., 2002; Rouchy and Caruso,

52   2006; Drinia et al., 2007; Moisette et al., 2018; Zachariasse et al., 2021; Kontakiotis et al., 2022).

53   Indeed, the MSC onset is often marked by the disappearance of foraminifers and CN in many

54   Mediterranean successions; such bioevent has been traditionally used as an indirect biostratigraphic

55   marker that best approximates the MSC onset (e.g. Sprovieri et al. 1996, Blanc-Valleron et al. 2002;

56   Manzi et al. 2007, Gennari et al., 2013; Violanti et al., 2013; Gennari et al., 2018; Manzi et al., 2016;

57   Manzi et al., 2018). However, the diachronous nature of the disappearance of CN and foraminifers

58   with respect to the MSC onset was observed in sections of the Piedmont and Sicily basins (Violanti et

59   al., 2013; Dela Pierre et al., 2014; Catalano et al., 2016; Sabino et al., 2020; Gennari et al., 2020).

60   Interestingly, in the Piedmont sections the disappearance of CN and foraminifers is associated with

61   the disappearance of reworked specimens of CN and foraminifers (i.e. from older stratigraphic

62   intervals such as Paleogene and Cretaceous) (Dela Pierre et al., 2014; Lozar et al., 2018; Gennari et

63   al., 2020), although sediment reworking is well recorded after the onset of the MSC (e.g. Natalicchio

64   et al., 2019; Sabino et al., 2020) and should have led to the presence of reworked calcareous tests as

65   well. In this light, the absence of calcareous tests, including those reworked from older stratigraphic

66   levels, may be related to diagenetic processes causing the preferential dissolution of biogenic calcite,

67   thereby suggesting that the disappearance of marine calcareous fossils was not caused by the

68   establishment of lethal environmental conditions in the water mass and at the seafloor (Dela Pierre et

69   al., 2014; Gennari et al., 2020). Furthermore, several evidences based on fossil occurrence during the

70   Primary Lower Gypsum (PLG) phase (i.e. CN, foraminifers, molecular fossils, diatoms, fishes, and

71   echinoids; Landini and Sorbini, 1989; Lacour and Néraudeau, 2000; Néraudeau et al., 2002;

72   Carnevale et al., 2019; Pellegrino et al., 2021) argue against a biotic crisis associated with the MSC

73   onset. Although the MSC time interval coincides with the absence of foraminifers (i.e. Non

74   Distinctive Zone, recently reviewed by Lirer et al., 2019), in SE Spain (Sorbas and Bajo Segura

75   Basins), calcareous micro and nannofossils were recorded in the marly hemicycles of the PLG unit

76   (Van de Poel, 1992; Riding et al., 1998; Goubert et al., 2001; Corbí and Soria, 2016). Such fossils

77   were considered as autochthonous, since evidence of reworking (e.g. abrasion, dissolution and

78   fragmentation of the tests) were not recognised (Corbí et al., 2016).

79   In order to shed light on the cause of the disappearance of the calcareous fossils at the onset and

80   during the first phase of the MSC, as well as on the paleoenvironmental conditions during this critical

81   interval of the Mediterranean history, we studied a composite section in the Sorbas Basin (Spain),

82   encompassing the pre-evaporitic to evaporitic transition and the PLG, in the frame of a well-

83   established astrochronologic age model (Krijgsman et al., 1999; Sierro et al., 2001; Krijgsman et al.,

84   2001; Manzi et al., 2013). Our reconstructions were based on detailed analyses of the

85   micropaleontological assemblages of laminated marl, marlstone, clay and carbonate layers recording

86   the pre-MSC/MSC transition and of the marly interbeds of the PLG unit. Micropaleontological

87   investigations on abundance and preservation of CN and foraminiferassemblages were complemented

88   by mineralogical, petrographic, element composition and carbon and oxygen stable isotope analyses

89   of the same sediments.

90

2- Geological setting

92   The Sorbas Basin is a small and narrow Neogene Basin surrounded by elongated basement ridges

93   forming the Sierra the Los Filabres, Sierra Alhamilla and Sierra Cabrera (Fig. 1). The Messinian stage

94   in the Sorbas Basin is recorded by the Caños Formation, which is subdivided into four members: the

95   Abad, Yesares, Sorbas and Zorreras members (Ruegg, 1964; Volk, 1967). The Abad Member was

96   deposited in the basin depocenter (estimated paleodepth of 400±100 m; Krijgsman et al., 2006) and

97   records the Tortonian/Messinian boundary at its base (Sierro et al., 2001); toward the northern and

98   southern basin margins, the sediments of the Abad Member pass to reefal limestone (Roveri et al.

99   2009). The Abad Member is divided into two units showing a precession-driven cyclical stacking

100   pattern: the Lower Abad (LA), characterized by the alternation of white and grey marls, and the

101   Upper Abad (UA), characterized by the alternation of sapropel and diatomite layers sandwiched

102   between white massive marls (Sierro et al., 2001; 2003). The Abad Member is overlain by the Yesares

103   Member through a sharp but stratigraphically continuous boundary (Manzi et al., 2013; Mancini et al.,

104   2020), which was interpreted by some authors as an erosional surface (Riding et al., 1998; Braga et

105   al., 2006; Bourillot et al., 2009). The Yesares Member corresponds to the local equivalent of the PLG

106 unit (Roveri et al., 2014) and is characterized by up to 16 lithological cycles composed of laminated

107 marl and gypsum or carbonate couplets (Dronkert et al., 1976; Krijgsman et al., 2001; Lugli et al.,

108 2010; Roveri et al., 2020); the base of the first gypsum bed marks the MSC onset at 5.971 Ma (Manzi

109 et al., 2013). Gypsum and carbonates are thought to reflect relatively more arid climate at precession

110 maxima, whereas marls were deposited during more humid phases at precession minima (Krijgsman

111 et al., 2001). A palaeodepth of ~ 150 - 240 m at the base of the Yesares gypsum has been estimated

112 based on benthic foraminifers (BF) and considering the difference of elevation between the top of the

113 uppermost pre-MSC reef layer and the first gypsum bed (Dronkert, 1976; Troelstra et al., 1980; van

114 de Poel, 1992; Riding et al., 1998; Baggley, 2000; Clauzon et al., 2015; Modestou et al., 2017). An

115 oolite and microbialite-dominated carbonate platform, referred to as the Terminal Carbonate Complex

116 (TCC, Fortuin and Krijgsman, 2003; Roveri et al., 2009; Clauzon et al., 2015), represents the shallow

117 water marginal equivalent of the Yesares Member (Roveri et al., 2020). The transition between the

118 Yesares and Sorbas members reflects a shallowing upward trend responsible for the establishment of

119 coastal environments in most parts of the Sorbas Basin (Krijgsman et al., 2001) and the eastward

120 progradation of deltaic and coastal wedges along the basin axis, with lagoon and beach deposits at the

121 top (Roep et al., 1998). Based on sedimentological observations, the palaeodepth of the basin at the

122 Yesares/Sorbas members transition can be estimated at 75 to 100 m (Krijgsman et al., 2001; Roveri et

123 al., 2020). The Sorbas Member underlies the continental deposits of the Zorreras Member, which

124 consists of reddish silts and interbedded lacustrine limestones. The Zorreras Member represents the

125 local expression of the last stage of the MSC (5.55-5.33 Ma), and also records the Messinian/Zanclean

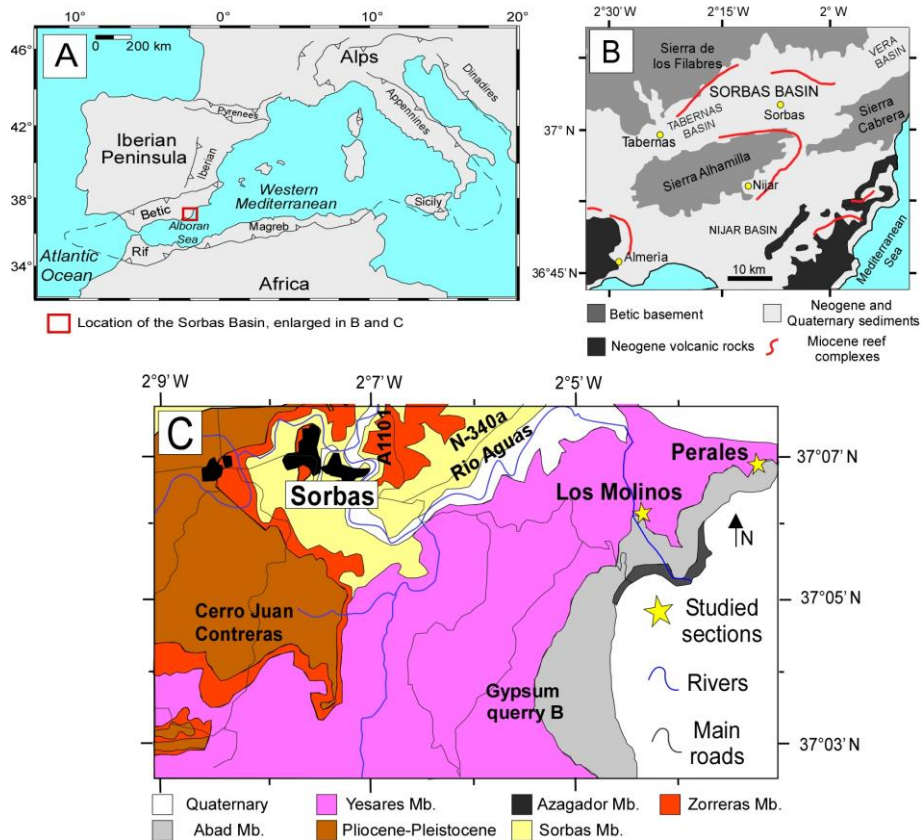126 boundary (Roveri et al., 2019).

127

128

Fig. 1: A: Location of the Sorbas Basin in the Mediterranean region (modified from Corbí and Soria, 2016). B: Simplified geological map of SE Spain showing the location of the Sorbas Basin (modified from Buorrillot et al., 2009). C: Geological map of the Sorbas Basin and location of the studied sections (modified from Roveri et al., 2020)

3- Material and methods

3.1. Studied sections and sampling

3.1.1 Perales section

The Perales section (37°05′49″N; 2°03′19″W) records the complete succession of events from the base of the Messinian (Abad Member, Sierro et al., 2001) to the lower 2 PLG cycles (Yesares Member, Manzi et al., 2013). The UA is characterized by quadripartite lithological cycles (laminated sapropel, lower homogeneous marl, diatomite, upper homogeneous marl) deposited under precessional control and under specific oceanographic and environmental conditions (stage 1 to 4 of Sierro et al., 2003; Mancini et al., 2020). An important lithological change is recorded in the uppermost pre-evaporitic cycle UA34, in which the "classical" lithological cycles that characterize the UA are replaced by brown organic rich marls with alternating poorly and finely laminated intervals, intercalated by a spiculite layer and two limestone beds (Fig. 2); therefore, the thickness of the organic rich marls in the cycle UA34 is greater compared to the underlying cycles. Calcareous fossils

148   sharply disappear in the uppermost limestone layer (Mancini et al., 2020), which is followed by a

149   blue/grey clay interval. This thick (2.7 meters) and anomalous lithological cycle precedes the

150   lowermost PLG cycle, made up of dark brown laminated marl and a laterally discontinuous gypsum

151   layer up to 3 m thick. The base of this layer is interpreted to correspond to the onset of the MSC in the

152   Perales section (Manzi et al., 2013). The gypsum bed of cycle PLG2, 7 to 10 meters thick, is

153   composed of laminated marl and laterally continuous massive selenite. Samples of the pre-MSC

154   interval up to PLG1 are the same reported in Mancini et al., (2020).
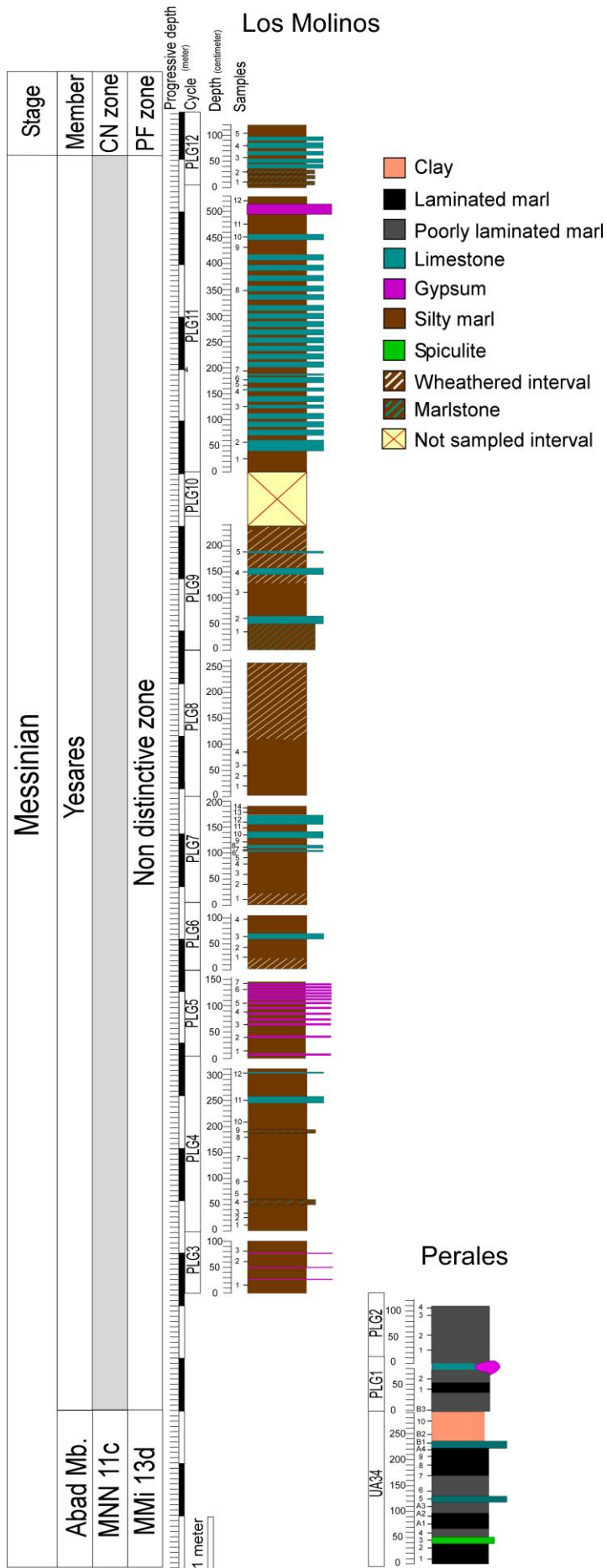
155   **3.1.2 Los Molinos section**

156   The Los Molinos section (37°5'53''N; 2°4'39''W) is located to the North of the Los Molinos de

157   Rio Aguas village (Fig. 1) along a canyon cut into the gypsum beds of the Yesares Member that

158   comprises different gypsum lithofacies (i.e. massive, banded and branching selenite; Lugli et al.,

159   2010). The marly hemicycles of the PLG unit are composed of laminated silty marl, marlstone

160   (consolidated laminated silty marl) and limestone (Fig. 2; supplementary material Fig. 1). No

161   erosional contacts were observed in the field. The thickness of the gypsum beds decreases upward, as

162   observed in the PLG unit of other Mediterranean sub-basins (Lugli et al. 2010). The section starts

163   from the second PLG cycle, but the total number of cycles is controversial, ranging from 13 (Dronkert

164   et al., 1976) to 15 (Krijgsman et al., 2001) or 16 (Roveri et al., 2009). This inconsistency raises from

165   the different interpretation of the upper part of the section, in which the recognition of the lithological

166   cyclicity is not straightforward. Indeed, in cycle PLG11 the laminated marls are replaced by micritic

167   limestones with unusual thickness (5 meters) compared to the other marly PLG hemicycles

168   (commonly 1.5 – 2 meters) (Fig. 2). Krijgsman et al. (2001) subdivided such thick micritic limestone

169   interval into three precessional cycles; Roveri et al. (2009) confirmed this interpretation on the basis

170   of the presence of discontinuous gypsum layers within the micritic limestone interval. Since we did

171   not recognise neither any significant lithological and colour change, nor any gypsum layer in the

172   micritic limestone interval, we considered this interval as representing a single hemicycle (Fig. 2). In

173   addition, the counting of the PLG cycles in the upper part of the section was also hampered by the

174   vegetation cover and by the thinning of the gypsum beds, often present as isolated outcrop spots. In

175   this section we collected 61 samples in the marl/limestone hemicycles (Fig. 2). We were unable to

176   sample cycle PLG10 because the outcrop was not accessible.

177

178

179

Los Molinos

Stage	Member	CN zone	PF zone
Messinian	Yesares	MNN 11c	MMi 13d
	Abad Mb.		

Non distinctive zone

Progressive depth (meter)

Cycle

Depth (centimeter)

Samples

PLG12, PLG11, PLG10, PLG9, PLG8, PLG7, PLG6, PLG5, PLG4, PLG3

Legend:
- Clay
- Laminated marl
- Poorly laminated marl
- Limestone
- Gypsum
- Silty marl
- Spiculite
- Wheathered interval
- Marlstone
- Not sampled interval

1 meter

Perales

PLG2, PLG1, UA34

180

181 Fig. 2: Composite stratigraphic column of the studied succession. Cycle PLG10 was not sampled.

182

183

3.2 Calcareous nannofossils analysis

A total of 97 samples of laminated marls, marlstones, clays, and limestones (Fig. 2) were
processed with the standard smear slides technique (Bown and Young, 1998) for the CN relative
abundance study. Particular attention was paid to the smear slide preparation procedure in order to
avoid contamination between samples, since the presence/absence of even small amounts of CN is a
relevant parameter in this study. Excluding completely barren samples, at least 400 CN specimens
were identified and counted at 1250× by polarized light microscopy in each slide; the reworked
species from older stratigraphic interval were counted separately and thereafter included in the total
CN counted. The taxa *S. abies* and *Sphenolithus moriformis* were grouped together in the informal
group *Sphenolithus* gr. Since the marine fossil record in PLG deposits was often considered as the
result of reworking from older sediments (Trenkwalder et al., 2008; Karakitsios et al., 2017), our
analysis aimed at assessing the potential reworked nature of the CN and, more generally, of the entire
micropaleontological assemblage. Accordingly, we assume that the presence of intact coccosphere
and/or the preservation of dissolution prone species (i.e. *Syracosphaera pulchra*, *Pontosphaera* sp.,
according to Roth and Berger, 1975; Roth and Coulbourn, 1982; Gibbs et al., 2004) are likely
indicative of *in-situ* assemblages, suggesting moderate or no reworking.

3.3 Microfossil analysis

A total of 57 samples of laminated marls, marlstones, clays and limestones from the Los Molinos
and Perales sections (Fig. 2) were prepared for microfossil (benthic and planktic foraminifers and
ostracods) investigation at the light microscope. About 100 g of oven-dried sediment were soaked in
diluted H_2O_2 for 1 day, and dry-sieved to obtain 3 different size fractions: > 500 µm, $500 - 125$ µm
and $125 - 63$ µm. Since foraminifer abundance and preservation were often scarce, we described
samples by means of qualitative observations separately on the 125 - 500 µm and 63 - 125 µm
residues.

3.4 Petrographic and mineralogical analyses

A total of 11 thin sections were obtained from epoxy impregnated samples cut parallel and
perpendicular to the bedding. Optical microscope observations of the thin sections were performed
using an Olympus BX51. Two representative thin sections of laminated samples were observed using
a Nikon microscope equipped with a B-2a filter block (illumination source with an excitation
wavelength of 450–490 nm). The thin sections were carbon coated and analyzed with a JMS-
IT300LV Scanning Electron Microscope (SEM). Semi-quantitative characterization of the main

215 elements was performed during SEM investigation using an energy-dispersive EDS Oxford
216 Instrument Link System microprobe. Elemental compositional maps were obtained from selected area
217 using the software Inca (acquisition time one hour, Cts > 130000). Additionally, one or two
218 representative stubs from freshly broken sediment chips from each precessional cycle were prepared
219 for morphological investigations. Morphological investigations were also performed on hand-picked
220 microfossils (benthic and planktic foraminifers and ostracods).

221 The laminated sediments from cycles PLG4 and PLG7 show alternation of white and brown
222 laminae; the white laminae from 11 samples were scraped using a tiny needle and then powdered
223 using an agate mortar. Powders of limestone beds belonging to the PLG6, PLG7, PLG9 and PLG11
224 were obtained as well using the same procedure. The powders were successively analyzed with X-Ray
225 Powder Diffraction (XRPD). Measurements for the raw identification of the crystalline phases were
226 carried out using a Rigaku MiniFlex 600 benchtop X-ray diffractometer (Bragg-Brentano geometry,
227 CuKα radiation, X-ray source operating at 600W (40 kV, 15 mA); D/teX Ultra2 silicon strip detector;
228 $2° < 2θ < 50°$, step width 0.01°, scan speed 5 °/min).

3.5 Carbon and oxygen stable isotope analyses

230 An aliquot (~ 300 μg) of the same powder samples prepared for XRPD analyses was used for
231 stable oxygen and carbon isotope analyses using an automated carbonate preparation device
232 (Gasbench II) and a Thermo Fisher Scientific Delta V Advantage continuous flow mass spectrometer.
233 Carbonate powder samples were reacted with > 99% orthophosphoric acid at 70°C. The carbon and
234 oxygen isotope bulk compositions are expressed in the conventional delta notation calibrated to the
235 Vienna Pee-Dee Belemnite (V-PDB) scale by the international standards IAEA 603 and NBS-18.
236 Analytical reproducibility for these analyses was better than ± 0.1‰ for both $δ^{18}O$ and $δ^{13}C$ values.

237

4- Results

4.1 Calcareous nannofossils

4.1.1 Perales section

241 Calcareous nannofossil content of the pre-MSC sediments from the Perales section and its
242 paleoenvironmental meaning were described in detail in Mancini et al. (2020). Cycle UA34 records
243 the MSC onset bioevent, coinciding with a relevant increase in the CN absolute abundance (Mancini
244 et al., 2021). Above this bioevent the assemblage is dominated by *Coccolithus pelagicus* and
245 *Reticulofenestra pseudoumbilicus* (supplementary material Fig. 4). The preservation of CN from the
246 MSC onset bioevent to the base of cycle PLG1 progressively decreases, as highlighted by dissolution
247 features (e.g. etching) affecting coccoliths (mostly *Helicosphaera carteri* and *C. pelagicus*). From the

248 second limestone bed of cycle UA34 (Fig. 2) up to cycle PLG2, CN are absent. Interestingly,
249 reworked specimens from older stratigraphic intervals, usually present in the UA cycles with variable
250 percentages (0.4 -23.6 %, average = 4.6 %; supplementary material Fig. 4), were not observed in the
251 barren samples of this interval.

252 **4.1.2 Los Molinos section**

253 In the Los Molinos section, CN are present in 36 out of 61 samples. The abundance and diversity
254 of the CN are generally lower than in the UA samples, except for a few samples with higher
255 concentration and a more diversified assemblage in cycles PLG4, PLG6, PLG7 and PLG9 (Fig. 3).
256 The CN preservation is generally poor, as revealed by dissolution features affecting coccoliths, such
257 as etching affecting the external rim and central area and fracturing (Fig. 4c, supplementary material
258 Fig. 8c). Overall, the CN assemblage is dominated by *Reticulofenestra minuta*, followed by other
259 reticulofenestrids, *H. carteri*, *Sphenolithus* gr. and *C. pelagicus*. *Umbilicosphaera rotula* and
260 *Umbilicosphaera jafari* are present with moderate to low abundance. The abundance of reworked
261 specimens is generally low (2% on average) and rarely exceeds 5%. In one sample (PLG4 sample 2),
262 both dissolution prone CN and intact coccospheres (*R. minuta*, *R. haqii*, *U. jafari*, *H. carteri*, *C.
263 pelagicus*) are present (Fig. 3).

264 It is worth noting that all the samples devoid of possible *in situ* assemblages are also characterized
265 by the absence of reworked specimens. In particular, samples from cycles PLG1, PLG2, PLG5 and
266 PLG8 are completely barren of both synsedimentary and reworked CN.

267 **4.2 Microfossils**

268 We include in this chapter qualitative and semi-quantitative analyses of foraminifer specimens
269 observed in washing residues at the optical microscope and at the SEM.

270 **4.2.1 Perales section**

271 Approximately from cycle UA27 upward (~ 6.15 Ma), the planktic foraminifers show a substantial
272 decrease in the preservation state, with an increase of the specimens affected by encrustation and
273 dissolution of external wall and by sediment/mineral infills (Reghizzi et al., 2017; Mancini et al.,
274 2020). Similar features were also observed in the Eastern Mediterranean from the
275 Tortonian/Messinian boundary to the MSC onset (Crete Island, Antonarakou et al., 2019). According
276 to the nomenclature adopted to describe the preservation state of planktic foraminifers (PF) proposed
277 by Antonarakou et al. (2019), from cycle UA27 to cycle UA34 the PF assemblage is dominated by
278 "chalky" specimens. Planktic foraminifers disappear below the first limestone bed of cycle UA34
279 (sample A3, Fig. 5), slightly below BF (Fig. 5). Benthic foraminifers are present up to the second
280 limestone bed of cycle UA34; within this cycle, they are exclusively represented by low-oxygen
281 tolerant bolivinids (*Bolivina spathulata* and *Bolivina dilatata*) and buliminids (*Bulimina aculeata* and

282 *Bulimina elongata*), among which *Bolivina dilatata* is dominant. From cycle UA27 upward, the shells

283 of BF are characterized by a progressive increase in dissolution, recrystallization and encrustation

284 features clearly visible at the SEM compared to BF recorded in the lower cycles (supplementary

285 material Fig. 2 and Fig. 3). SEM observations show the presence of abundant pyrite or oxidised pyrite

286 inside the foraminifer shell (Fig. 5 A3; supplementary material Fig. 3). In some cases, oxidised pyrite

287 was found to occupy a small void deriving from the BF shell dissolution (Fig. 5A4). From the second

288 limestone bed upward, foraminifers have not been observed in the washing residues.
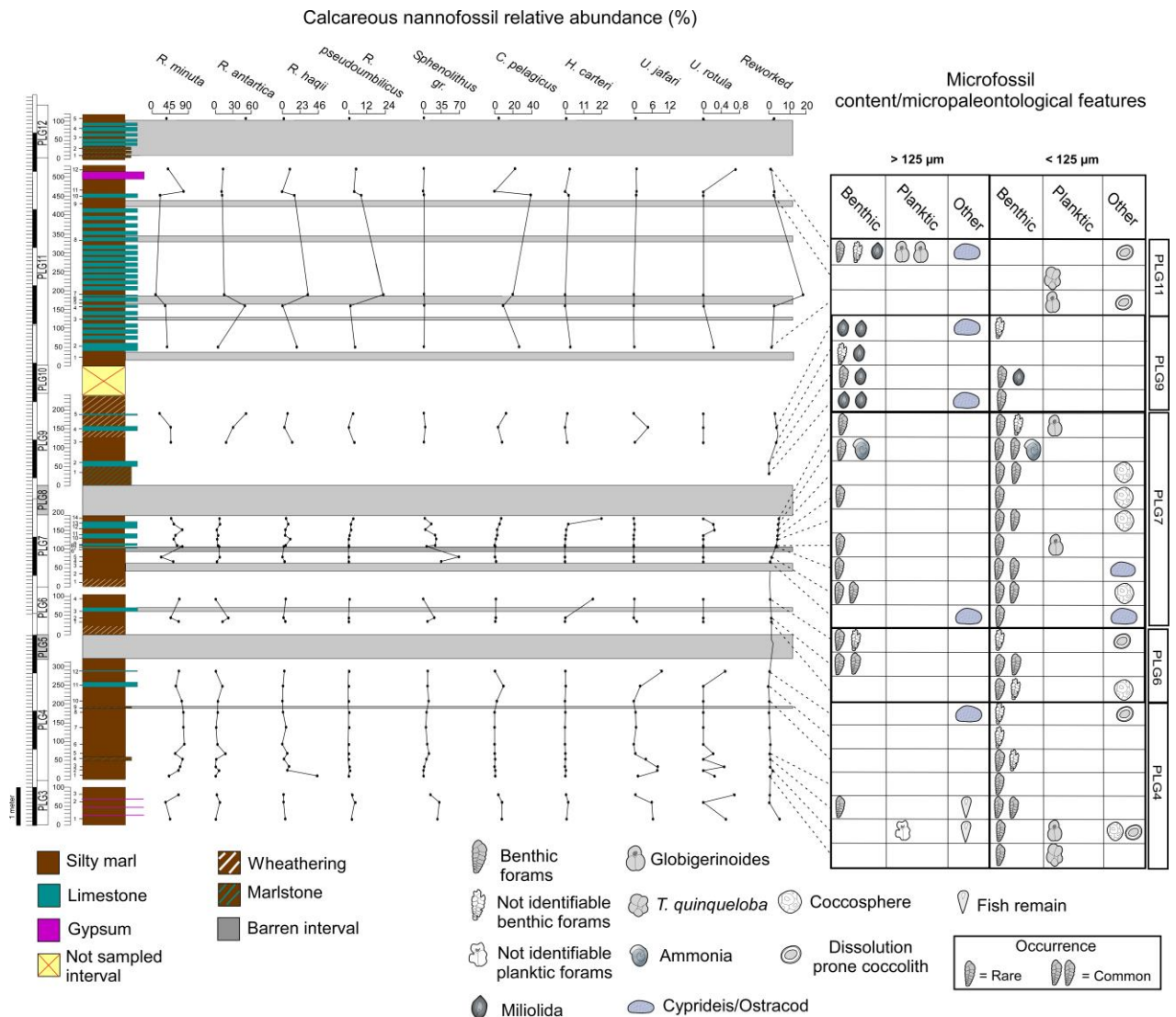
289 **4.2.2 Los Molinos section**

290 In the Los Molinos section, foraminifers (both 63 - 125 and > 125 μm size fraction) are generally

291 rare (PLG4, PLG7, PLG11 and PLG12) or absent (PLG3, PLG5 and PLG8) except in cycles PLG6

292 and PLG9 where some layers yield more abundant BF (Fig. 3). Preservation is generally scarce, with

293 specimens showing partial dissolution of the outer side of the wall, fragmentation and external

294 encrustation; pyrite framboids or oxidised pyrite infills were also observed (supplementary material

295 Fig. 8). According to the definition of preservation classes proposed by Antonarakou et al. (2019), the

296 recorded foraminifers are mostly "chalky". In some cases, the external encrustation of the tests

297 hampered the taxonomic identification at the species or even at genus level. Reworked taxa from

298 older stratigraphic interval were not recorded throughout the section. Detrital grains and bioclastic

299 materials are almost absent in the 63 – 125 μm size fraction.

300 In cycle PLG4, the >125 μm fraction of each sample is barren, while rare bolivinids, *Turborotalita*

301 *quinqueloba* and globigerinids are present in the smaller fraction of samples collected in the lower

302 half of the marly hemicycle (Fig. 3). All the samples of cycle PLG5 were barren of foraminifers in

303 both the size fractions. The basal sample of cycle PLG6 yields very rare and badly preserved BF in

304 the smaller-size fraction. Rare to common *Fursenkoina fusiformis* specimens are observed in the

305 middle of the marly interval of cycle PLG6 (Fig. 3), where the assemblage is nearly monospecific,

306 although some specimens of *B. aculeata* are also present in the <125 μm size fraction. Just above,

307 only few *Cribroelphidium* specimens and small bolivinids were observed. In cycle PLG7, barren

308 samples alternate with samples yielding rare *Globigerinoides* spp. and BF that are variably

309 represented by species of *Ammonia*, *Cribroelphidium*, *Bulimina* and *Bolivina* in both size fractions

310 (Fig. 3). Usually, the assemblages are oligospecific, except in cycle PLG7 (sample 13), where species

311 of these genuses co-occur. The samples from the marly interval of cycle PLG9, yield rare to common

312 miliolids, sometimes associated with disarticulated valves of the ostracod *Cyprideis* sp. (Fig. 3).

313 Cycles PLG11 yield prevalently barren samples, except in three samples in which common to rare PF

314 (*Globigerinoides* spp., *T. quinqueloba* and neogloboquadrinids) were observed; on the other hand,

315 benthic assemblage was recorded only in the uppermost sample in the >125 μm size fraction (Fig. 3).

316 Cycle PLG12 is barren of microfossils (Fig. 3)

317

318

Fig. 3: Micro and nannofossil content of Los Molinos section. Bolivinids, Buliminids, Uvigerinids, *Elphidium*, *Cibroelphidium* and *Fursenkoina* are grouped together and plotted as benthic foraminifers. Cycles PLG5 and PLG8 are barren of fossils; cycle PLG10 was not sampled.

## 4.3 Petrographic and taphonomic observations

SEM observations of polished thin sections and stubs allowed further characterization of the samples collected from cycles UA34 to PLG12. Pyrite has been found within and on the wall of certain individual of BF specimens, as well as in the sedimentary matrix (supplementary material Fig. 8E and Fig. 9B), which consists of clay, silt-sized terrigenous grains or micrite. Pyrite observed in the matrix is consistently small-sized (< 10 μm; supplementary material Fig. 8E, Fig. 9B and Fig. 9F). Pyrite and oxidised pyrite moulds (most likely after PF and BF) are present in cycle UA34 (Fig. 5 A3

331 and A3$_2$); these features increase in abundance upward in the section, becoming very common in the

332 second limestone bed of cycle UA34 (Fig. 5 B1, B1$_2$ and B1$_3$), although no PF, CN and BF were

333 observed through optical microscope observations of smear slides and washing residues. In some

334 cases, the calcitic test of foraminifers is either completely dissolved or replaced by calcite

335 microcrystals (Fig. 5 B1$_2$ and B1$_3$). Sparry calcite filling the foraminifer chambers was also rarely

336 observed (Fig. 5 B1$_3$). This limestone bed is overlain by a blue/grey clay bed characterized by very

337 low abundance of carbonate grains (supplementary material Fig. 6), as revealed by EDS analyses.

338 Sub-spherical Si-rich grains with a circular cross section (300 to 800 µm in diameter) surrounded by a

339 siliciclastic matrix were observed in this level. Rounded cavities with oxidised pyrite infill are also

340 present (Fig. 5 B2$_2$). Above the clay bed, the laminated marly hemicycle of cycles PLG1 and PLG2

341 still contains pyrite and oxidised pyrite aggregates, some of them with elongated shape resembling

342 normal size to dwarfed BF internal moulds (Fig. 5 B3).

343 The Los Molinos section is characterized by prevalently laminated silty marls with poorly preserved

344 calcareous fossils (CN, ostracods and foraminifers; Fig. 3 and Fig. 4 B, C, D, E and F; supplementary

345 material Fig. 8 A, B, C, D, E and F), although some levels were completely barren (Fig. 3). The marly

346 hemicycles of cycles PLG4 and PLG7, which yield rare to common BF, show peculiar features as

347 they host laminated silty marl typified by the alternation of sub-mm thick brown and white laminae

348 (Fig. 6). EDS analyses show that the brown laminae contain aluminosilicates composed of Mg, Si, Al

349 and K (Fig. 7). Calcareous nannofossils, aragonite (as revealed by XRPD analysis), calcite and pyrite

350 grains <5 µm are also present in these laminae as minor components. In contrast, the white laminae

351 are almost exclusively composed of aragonite, based on XRPD results (supplementary material Fig. 7)

352 (about 70% – 90% based on SEM qualitative observation), with CN and pyrite grains <5 µm as a

353 minor component. Aragonite crystals commonly show two habits: bladed crystals, about 10 µm long,

354 and acicular needles usually < 6 µm. Bladed aragonite sometimes is locally grouped to form clusters

355 of radially oriented crystals (supplementary material Fig. 9). The aragonitic laminae display 1 – 5 µm

356 large longitudinal cracks (Fig. 6 and Fig. 7). Celestite and barite were also sporadically observed

357 within the aragonitic laminae.
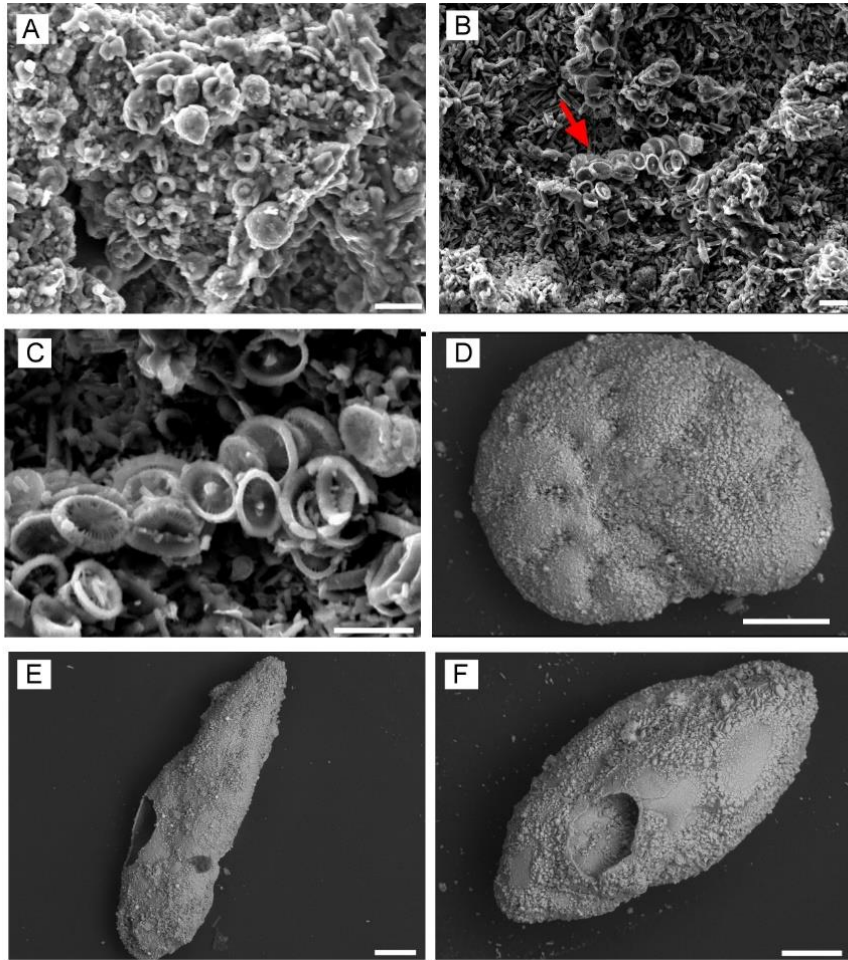
Fig. 4: SEM images of freshly broken sediment surface and hand-picked foraminifers from the Los Molinos samples. A: Fecal pellet mostly composed by CN (cycle PLG4). B: Disrupted coccosphere of *Syracosphaera pulchra* (red arrow) in an aragonitic matrix (cycle PLG7). C: close up of B; with a cluster of coccoliths of *Syracosphaera pulchra* showing dissolution and fracturing features. D: Benthic foraminifer showing calcite encrustation (cycle PLG7); oxidised pyrite is also present as a minor component of the encrustation E: Encrusted and fragmented *F. fusiformis* (cycle PLG6). F: A miliolid showing dissolution of the external wall and calcitic/pyritic encrustations (cycle PLG7).

4.4 C and O stable isotope analyses

The stable isotope results were plotted and compared with the stable isotope composition of the Great Bahamas Bank aragonite and with biological sourced aragonite (i.e. codiacean algae, *Halimeda* and skeletal material; Fig. 8). The aragonite laminae show positive $\delta^{13}C$ values ranging from +2.49 to +3.56 ‰ whereas the $\delta^{18}O$ values are slightly negative (from -2.28 to -0.25 ‰) (Fig. 8). The $\delta^{13}C$ and $\delta^{18}O$ values of the limestone layers belonging to cycles PLG6, PLG7, PLG9 and PLG11 fluctuate from -1.09 to +1.04 ‰ and from -4.75 to +4.73 ‰, respectively (Fig. 8). The lowest $\delta^{18}O_{limestone}$ values were recorded in cycles PLG9 and PLG11 (-3.73 and -4.75 ‰, respectively; Fig. 8), while limestones from cycles PLG6 and PLG7 showed higher values (+4.73 and -0.36 ‰, respectively).

5 Discussion

5.1 The influence of taphonomic processes on the distribution of calcareous micro and nannofossils.

The influence of taphonomic processes on the distribution of calcareous micro and nannofossils in the different intervals of the studied succession is discussed herein based on the whole micropaleontological, petrographical and isotopic dataset.

5.1.1 The pre-MSC/MSC transition

Several evidences suggest an upward increase of calcite dissolution starting from the base of cycle UA34:

a) the increase of the relative abundance of dissolution-resistant CN taxa (i.e. *C. pelagicus* and *R. pseudoumbilicus*; supplementary material Fig. 4) toward the MSC onset and the complete disappearance of CN in the second limestone layer of cycle UA34 (Fig. 5). *Coccolithus pelagicus* and *R. pseudoumbilicus* are among the most dissolution-resistant taxa (Roth and Berger, 1975; Roth and Coulbourn, 1982; Gibbs et al., 2004), thus their dominance, together with the absence of dissolution-prone CN specimens, suggests that the observed CN assemblage was likely influenced by dissolution of biogenic calcite.

b) The deterioration of the preservation quality of the calcareous microfossils with respect to the underlying cycles (Fig. 4, A4 and A4$_2$; supplementary material Fig. 2; Fig. 3).

c) The order of micro and nannofossil disappearance (PF, CN and finally BF) is fully consistent with laboratory and sediment trap observations showing that PF are more susceptible to dissolution than CN and BF (Peterson and Prell, 1985; Steinsund and Hald, 1994; Chiu and Broeker, 2008; Subhas et al., 2018). Our observations are therefore consistent with the notion that biogenic calcite in in the analysed samples was progressively dissolved.

d) The absence of reworked specimens of calcareous fossils, that is in contrast with the evidence of sediment reworking at the MSC onset (e.g. Natalicchio et al., 2019; Sabino et al., 2020).

e) The presence of internal moulds of foraminifers filled with pyrite or oxidised pyrite (Fig. 5 A3, A3$_2$) in the layers recording the PF and BF disappearance in the washing residue. The dissolution of the calcitic wall of foraminifers led to the formation of empty cavities between the pyrite infill and the surrounding sediment (Fig. 5, A3). These features indicate that the foraminifer disappearance was related to the dissolution of the test, which likely occurred during early diagenetic phases in the taphonomically active zone. SEM observations show that the content in pyrite foraminifer moulds increases upwards, peaking in the second limestone layer of cycle UA34 (Fig. 4 B1 and B1$_2$; supplementary material Fig. 5) where no calcareous microfossils were observed in washing residues

409 and smear slides. Indeed, standard micropaleontological methods (i.e. disaggregation, treatment with
410 peroxide and the successive sieving of the sediment) result in the alteration of delicate sediment
411 components such as pyrite moulds, that can be unnoticed with optical microscope investigations of the
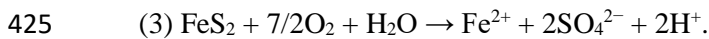412 washing residues and smear slides.

413 f) The total absence of carbonate grains in the blue clay level above the second limestone layer of
414 cycle UA34, suggesting the exacerbation of dissolution processes just below the first PLG cycle (Fig.
415 2).

416 g) Pyrite aggregates mimicking BF shape were observed in the marly hemicycles of cycles PLG1
417 and PLG2, suggesting intense carbonate dissolution also in these intervals (Fig. 5, B3)

418 The presence of oxidised pyrite moulds after foraminifers may reflects the degradation of organic
419 matter (i.e. foraminifer cytoplasm) through bacterial sulphate reduction in an anoxic
420 microenvironment, which took place within the foraminifer test either in the water column or at the
421 sea floor (Buckman et al., 2020) following the reactions:

422 (1) $2CH_2O + SO_4^{2-} \rightarrow H_2S + 2HCO_3^-$

423 (2) $Fe^{2+} + H_2S \rightarrow FeS_2 + H_2$.
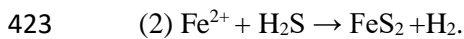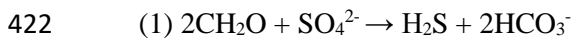
424 Subsequent pyrite oxidation, according to the reaction:

425 (3) $FeS_2 + 7/2O_2 + H_2O \rightarrow Fe^{2+} + 2SO_4^{2-} + 2H^+$.

426 Pyrite oxidation increases local acidity which could trigger dissolution of biogenic calcite (McNeil,
427 1997; Buzas-Stephens and Buzas, 2005; Liu et al., 2018) as observed in our material. Small sized
428 pyrite (<10 μm) was also consistently found in this interval, suggesting euxinic condition in the lower
429 water column (Bond and Wignall, 2010; Tagliavento et al., 2020).

430 Dissolution of biogenic calcite could also take place in aerobic conditions through the degradation
431 of organic matter, according to the reaction:

432 (4) $CH_2O + O_2 \rightarrow CO_2 + H_2O$.
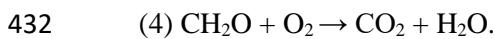
433 The production of CO_2 increases acidity, in turn promoting dissolution of biogenic calcite (Archer
434 and Maier-Reimer, 1994; Jahnke et al., 1997; Archer, 2003; Suárez-Ibarra et al., 2022) according to
435 the reaction:

436 (5) $CO_2 + CaCO_3 + H_2O + \leftrightarrow 2HCO_3^- + Ca^{2+}$.
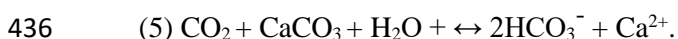
437 Based on these evidences, we suggest that the disappearance of biogenic calcite reflects a taphonomic
438 bias, related to the accumulation and the subsequent oxidation of pyrite and organic matter at the sea
439 floor.
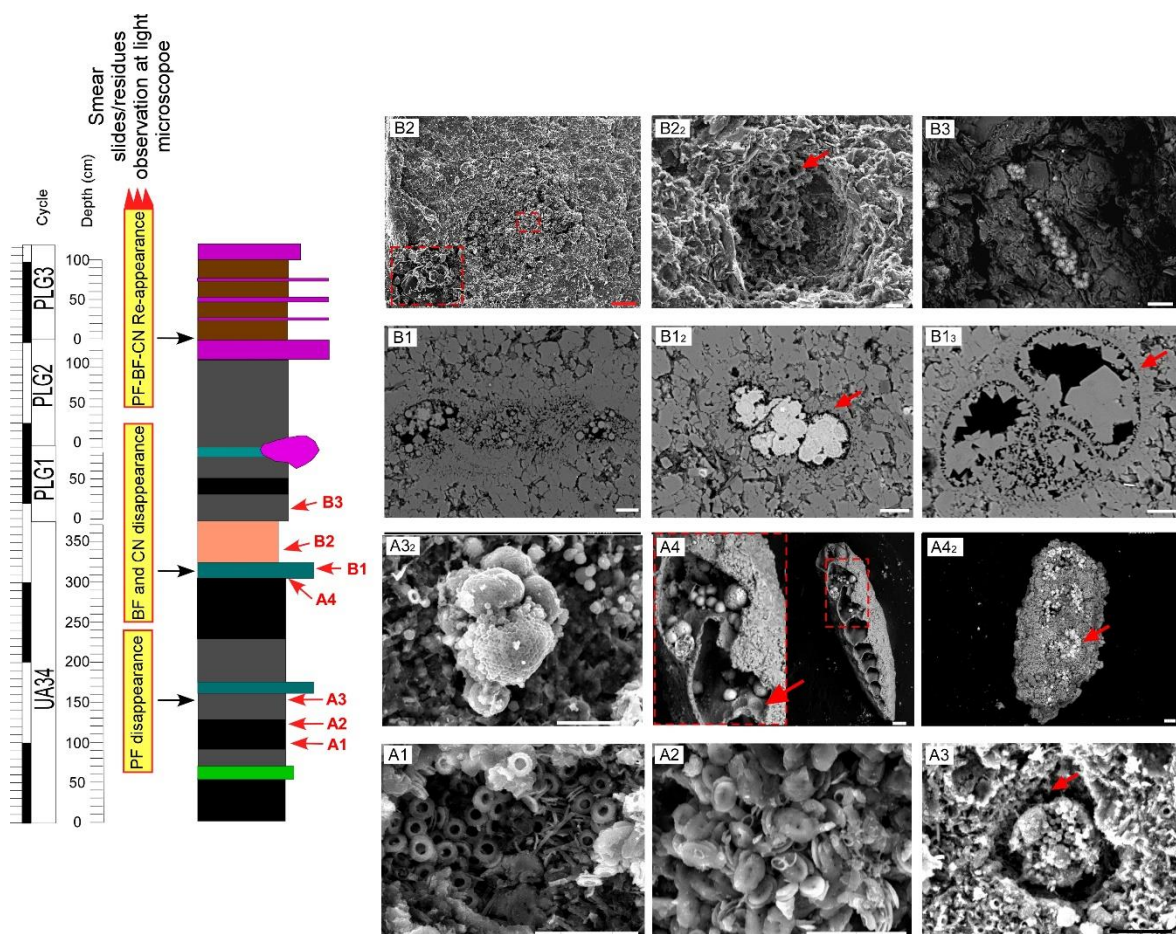
Fig. 5: Left: stratigraphic column of the interval encompassing the MSC onset in the Perales section with location of the samples recording the disappearance of the micro and nannofossils as observed in the washing residues and smear slides. On the right, SEM images from stubs or thin sections and from handpicked foraminifers. The red numbered letters in the stratigraphic section indicate the location of the samples. Gypsum layers of cycles PLG 2 and PLG3 are not to scale. A1: High abundance of *U. rotula* characterizing the MSC onset bioevent. A2: High abundance of *H. carteri* characterizing the MSC onset bioevent. A3: Putative pyrite mould after foraminifer. The red arrow indicates the empty space (previously occupied by the test) between the pyrite and the sedimentary matrix. $A3_2$: Putative pyrite internal mould after a dwarf foraminifer test, probably a Turborotalid. A4: Hand-picked benthic foraminifer belonging to the genus *Bolivina*. The specimen shows dissolution feature on the shell margin. Red arrows indicate oxidised pyrite that leaves dissolution pits on the internal calcitic wall. $A4_2$: Handpicked benthic foraminifers showing large calcitic encrustation and oxidised pyrite infills. Red arrow shows the boundary between the oxidised pyrite and the calcitic wall, the latter is partially dissolved. B1: Back scattered SEM images of polished thin section showing a dissolved phosphatic fish remain with oxidised pyrite infills. $B1_2$: Back scattered SEM images of polished thin section showing a putative pyrite mould after a foraminifer. Red arrow shows the replacement of the original calcitic wall with fine grained calcite. $B1_3$: Back scattered images of polished thin section showing a foraminifer with large calcitic crystals close to the wall. Red arrow indicates the highly altered foraminifer wall. B2: SEM image of freshly broken sediment surface of the blue/grey clay interval, showing a rounded cavity filled with quartz crystals and surrounded by a siliciclastic matrix. The carbonate component of this layer is nearly absent (supplementary material Fig. 6). $B2_2$: Void with oxidised pyrite with honeycomb structure. B3: Oxidised pyrite mimicking a dwarf benthic foraminifer. Scale bar is 20 μm, except in B2, in which is 100 μm

5.1.2 The PLG unit

Rare to common foraminifers and CN are discontinuously present from cycle PLG3 upward (i.e. 5.93 Ma onward), still showing dissolution evidence and a variable degree of preservation (Fig. 4; supplementary material Fig. 8). On the other hand, the content of organic matter and oxidised pyrite

464   in the sedimentary matrix and in the foraminifer chambers is significantly lower compared to the

465   underlying sediments. Such observation agrees with the notion that the preservation of biogenic

466   calcite is tightly linked with oxidation of pyrite and of organic matter (see paragraph 5.1.1).

467   Aragonite laminae were observed in the marly hemicycle of cycles PLG4 and PLG7. The

468   aragonite/calcite stability is mostly controlled by the Mg/Ca ratio in sea water (Morse et al., 1997;

469   Bots et al., 2011). In particular, if Mg/Ca > ~ 0.6–0.7, aragonite becomes the dominant phase, and

470   with values of ~1.7 only aragonite precipitates. The Mg/Ca ratio and the temperature control the

471   substitution of Mg^{2+} in the calcite lattice (Burton and Walker, 1991), which ultimately drives the

472   thermodynamic stability of calcite. In addition, Bots et al. (2011) showed that an increase in dissolved

473   SO_4^{2-} decreases the Mg/Ca ratio at which calcite is destabilized and aragonite becomes the dominant

474    $CaCO_3$ polymorph. We thus suggest that the presence of well-preserved aragonite and the contextual

475   poorly preserved biogenic calcite in cycles PLG4 and PLG7 may reflect an increase in dissolved Mg^{2+}

476   and SO_4^{2-} ions in the water column. This mechanism could represent an additional cause for the poor

477   preservation of micro and nannofossils in the PLG unit.

478
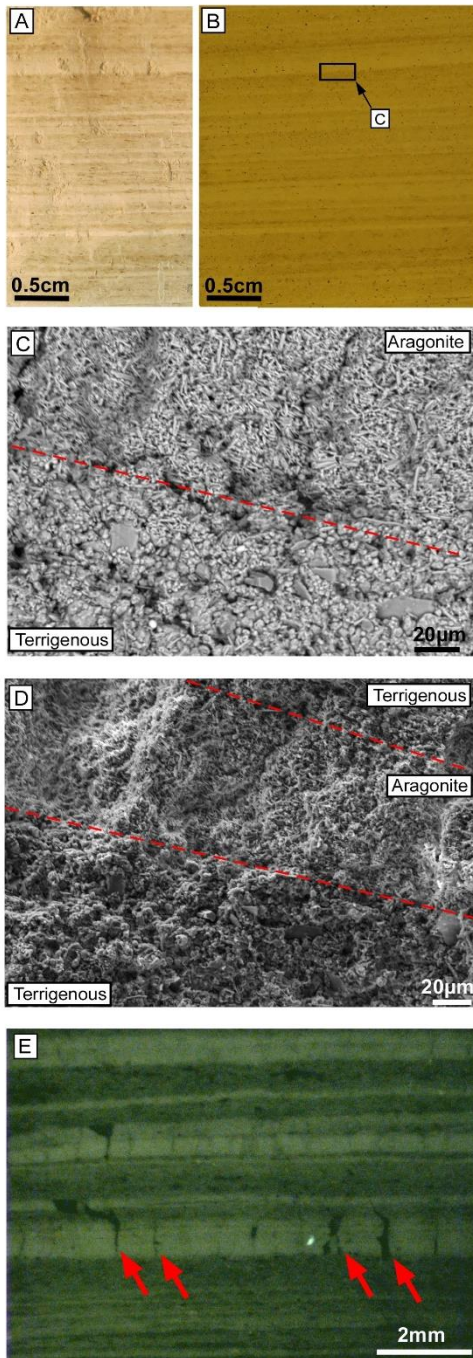
Fig. 6: The laminated marls from cycles PLG4 and PLG7. A: Polished slab of a freshly broken sediment chip. B: Photomicrograph
(transmitted light) of the same sample as in A; the black square shows the position of C. C: SEM image (polished thin section) showing the
alternation of the terrigenous and the aragonitic laminae. Note the longitudinal cracks in the aragonitic lamina; red dotted line defines the
boundary between the laminae. D: SEM image of freshly broken sediment showing the alternation of the terrigenous lamina and the
aragonitic lamina; red dotted line defines the boundary between the lamina. E: UV light photomicrograph of laminated sediment; note the
bright autofluorescence of the aragonite laminae and the vertical cracks (red arrows).

485
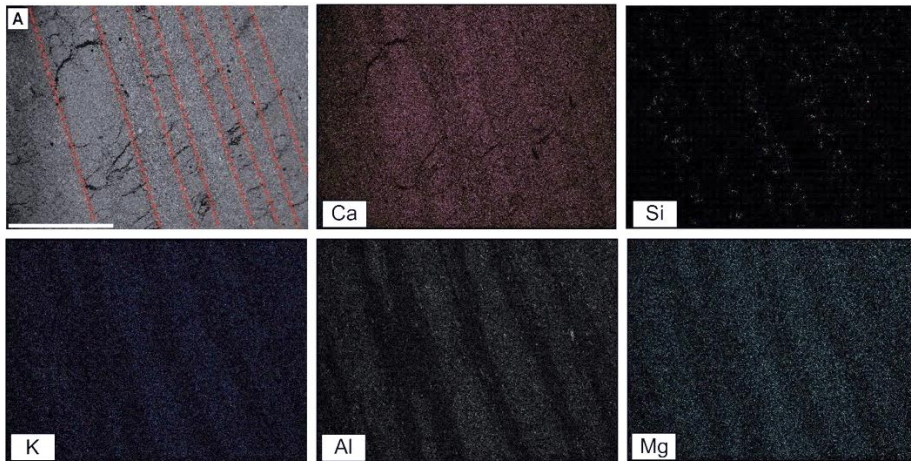
Fig. 7: Representative SEM images and elemental maps (Ca, Si, K, Al and Mg) of the laminated marls from cycles PLG4 and PLG7
(polished thin sections). A is the reference image; the red dashed lines indicate the lower and upper boundaries of the aragonite laminae.

486
487

488

5.2 Paleoenvironmental condition leading to the dissolution of calcareous tests

489

There are consistent evidences that the micro and nannofossil records of the uppermost pre-
evaporitic phase (cycle UA34) and of the PLG unit are biased by dissolution of calcareous tests
resulting from pyrite and organic matter oxidation and changes in Mg^{2+} and SO_4^{2-} content in seawater.
These processes were triggered by paleoenvironmental changes as recorded by sedimentological,
petrographical and micropaleontological data. Indeed, just prior to the MSC onset, cycle UA34
records an exceptional and prolonged increase of organic matter preservation (Fig. 2) during both
insolation maximum (wetter and warmer conditions) and minimum (drier and colder conditions),
marking a striking difference with respect to the older UA cycles, where grey homogeneous marls and
diatomites are intercalated between organic rich layers (Sierro et al., 2001). Apparently, in UA34,
warmer/wetter and drier/colder phases are recorded by the alternation of intervals characterized by
prevalent laminated or weakly laminated sediments, respectively (Fig. 2). This alternation created the
condition for pyrite formation and organic matter accumulation during phases of bottom anoxia and
water column stratification (warmer/wetter periods), and their subsequent oxidation during more
mixed conditions (drier/colder periods). Since the same climatic alternations are involved in the
"normal" UA cyclicity at the precessional scale (Sierro et al., 2003; Mancini et al., 2020) without any
strong evidence of dissolution of biogenic calcite, it is reasonable to hypothesize that the final
restriction of the basin (cycle UA34, just below the MSC onset) favoured calcite dissolution by
increasing the sensitivity to external (climatic) forcing, such as (seasonal) variation in the freshwater
input and temperature, which promoted fluctuations of bottom redox conditions.
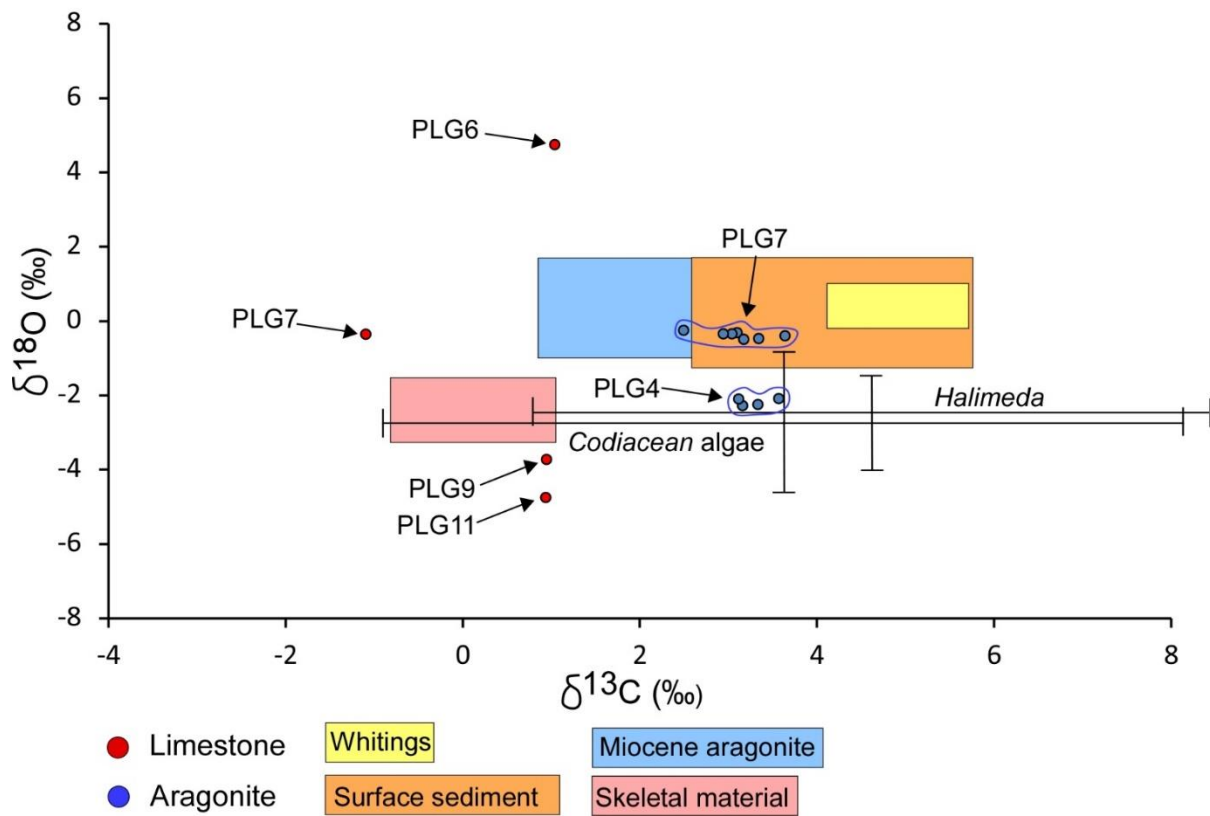
During the pre-evaporitic phase, several lines of evidence suggest a gradual progression
towards more restricted conditions (Kouwenhoven et al., 2006; Vasiliev et al., 2019; Kontakiotis et
al., 2019; Corbí et al., 2020; Zachariasse et al., 2021; Bulian et al., 2022; Kontakiotis et al., 2022).
Indeed, a Mediterranean scale restriction step increased organic matter accumulation at every

513   insolation maximum from 6.7 Ma (Sierro et al., 2001; Sierro et al., 2003; Mayser et al., 2017;

514   Kontakiotis et al., 2020; Kontakiotis et al., 2021). Similarly, toward the MSC onset increasing runoff

515   influence is suggested by the oxygen stable isotope composition of foraminifer tests from ~6.1

516   ($\delta^{18}O_{neogloboquadrinids}$ down to -4‰; Reghizzi et al., 2017). A freshening of the water column was

517   recorded also in the Eastern Mediterranean at the same time (Vasiliev et al., 2019). Finally, in cycle

518   UA34, the abundance peaks of *S. abies* and *H. carteri* (part of the MSC onset bioevent), both able to

519   thrive in freshwater-influenced environments (see Mancini et al., 2020), and the lithological changes

520   described above suggest enhanced influence of river runoff, promoting surface water freshening,

521   nutrient input, water column stratification and high productivity (Mancini et al., 2021). We infer that

522   marked climate-induced fluctuation of oxygen content at the bottom took place, promoting pyrite

523   formation and organic matter preservation during anoxic phases (wet/warm season; Fig. 9A), and their

524   successive oxidation during oxygenated phases (arid/cold season; Fig. 9B). These mechanisms,

525   involving a marked fluctuating oxycline, likely led to the progressive dissolution of foraminifers and

526   CN toward the MSC onset (Fig. 9A and Fig. 9B). Carbonate dissolution reached the acme in the blue

527   clay level (Fig. 2), that is almost devoid of carbonate grains (supplementary material Fig. 6). Although

528   the lack of carbonate grains should be investigated with greater detail, the concomitant absence of

529   reworked calcareous taxa suggests that such a pattern is not the result of a biocalcification reduction,

530   as previously suggested (Blanc-Valleron et al., 2002; Rouchy and Caruso, 2006). At the beginning of

531   the MSC, sediments of cycles PLG1 and PLG2 still yield pyrite moulds, but their link with BF is not

532   straightforward. Thus, the absence of calcareous microfossils in washing residues and smear slides

533   cannot be unambiguously interpreted in terms of a taphonomic bias. However, marine fossils (fishes,

534   echinoids, bivalves, bryozoans and gastropods) were recorded in coeval shallower sediments from the

535   Sorbas Basin (Los Yesos section, Montenat et al., 1980; Saint Martin et al., 2001; Goubert et al.,

536   2001; Néraudeau et al., 2002) and neighbouring basins (Carboneras-Nijar Basin, Van de Poel, 1992).

537   Indeed, in the more marginal and shallow part of these basins (i.e. Los Yesos), the mixed layer

538   delivering oxygen could have reached the sea bottom, hampering pyrite and organic matter

539   accumulation. From cycle PLG3 upward, decreased pyrite and organic matter accumulation was

540   possibly responsible for improved preservation of calcareous micro and nannofossils which, however,

541   still show dissolution evidence (Fig. 3, Fig. 4; supplementary material Fig. 8). The presence of

542   aragonite in some cycles and the poor preservation of calcite fossils could reflect an increase of

543   dissolved Mg^{2+} and SO_4^{2-} ions in seawater (paragraph 5.1.2). Although additional investigations are

544   needed to constrain the sources of Mg^{2+} and SO_4^{2-}, the CN assemblage (for more detail, see 5.4

545   paragraph) supports the hypothesis that the SO_4^{2-} and the Mg^{2+} were river-delivered, since taxa such as

546   *H. carteri*, *Sphenolithus* gr. and *C. pelagicus*, adapted to low salinity conditions (Giraudeau et al.,

547   1992; Silva et al., 2008; Auer et al., 2014; Mancini et al., 2020) are common in these layers (Fig. 3).

548   In particular, among these taxa, *C. pelagicus* was observed to thrive at salinity down to 26.5 ‰ (Silva

et al., 2008).

5.3 The aragonite and its paleoenvironmental significance

The aragonite crystals found in the laminated deposits of the marly hemicycles of cycles PLG4 and PLG7 display shape and size similar to the Bahamas aragonite (Loreau, 1982, page 39 Fig. d; Shinn et al., 1989, Fig. 9 a, b, c and d; MacIntyre and Reid, 1992, Fig. 1 a and b; Milliman et al., 1993, Fig. 2 a, b and c). The slightly negative $\delta^{18}O$ values (from -2.28 to -0.25 ‰) of the studied aragonitic laminae suggest that aragonite did not precipitate from evaporated sea water; in this case, positive values (up to 9‰) should be expected (Ziegenbalg et al., 2010). Aragonite is ^{13}C-enriched ($\delta^{13}C$ values from +2.49 to +3.56 ‰) compared to the present-day Mediterranean surface water ($\delta^{13}C$ +0.96 to +1.52 ‰; Pierre, 1999) and Tortonian bulk calcite from Lorca Basin, SE Spain ($\delta^{13}C$ -1.8 to +0.2 ‰ Pierre and Rouchy, 2004). Such ^{13}C enrichment may reflect intense photosynthetic activity in the upper water column; indeed, photosynthesis preferentially removes ^{12}C causing the water to become enriched in the heavier ^{13}C isotope (Robbins and Blackwelder, 1992; Swart and Eberli, 2005; Swart et al., 2009). Therefore, we suggest that aragonite precipitation in the water column of the Sorbas Basin could have been induced by autotroph blooms (Robbins and Blackwelder, 1992; Obst et al., 2009;

572   Swart et al., 2009;; Sondi and Juračić, 2010) which decreased the local pCO$_2$ and increased alkalinity,

573   favouring the precipitation of carbonate minerals (calcite and aragonite) (Larson and Mylroie, 2014).

574   Aragonite-rich deposits were observed across the MSC onset and during the first MSC phase in Sicily

575   (Italy), but their different isotopic signature (δ^{13}C values from -49 to -36 ‰ and δ^{18}O values from +5

576   to +5.6 ‰, Zieglenblag et al., 2010; δ^{13}C from -1 to +1.9 ‰ and δ^{18}O from +3 to +7.4 ‰, Perri et al.,

577   2017) with respect to the crystals studied here, suggests a different origin. On the other hand, the

578   isotopic signature of the Sorbas Basin aragonite is similar to that of Middle Miocene and modern

579   sediment of the Great Bahamas Bank (Fig. 8; Shinn et al., 1989; Turpin et al., 2011). Therefore, we

580   suggest that possible analogues of the Sorbas Basin aragonite are the so-called "whiting" of the Great

581   Bahamas Bank (Robbins and Blackwelder, 1992; Swart et al., 2009). Localised aragonite precipitation

582   can also take place within extracellular polymeric substance (i.e. EPS) (Obst et al., 2009) produced by

583   picoplankton, phytoplankton and green algae (Yates and Robbins, 1998). In modern environments,

584   aragonite can be also biogenically produced by algae (e.g. *Halimeda*), with isotopic signature in the

585   range of our results (Fig. 8), but the habit of the resulting crystals differs from that of the crystals

586   deriving from whitings (Lorau, 1982; MacIntyre and Reid, 1992; Shinn et al., 1989; MacIntyre and

587   Reid, 1995). Aragonite microcrystals from *Halimeda* are 3 to 10 μm long and show sharp-faced

588   crystals and blunt terminations; in addition, the majority of crystals produced by *Halimeda* are in the

589   form of nanograins ($\simeq$ 1 μm; MacIntyre and Reid, 1992). Despite *Halimeda is* widely reported in

590   carbonate platform deposits surrounding the Sorbas Basin at the time of PLG deposition (Roveri et al.,

591   2009; Roveri et al., 2020), the habit of the studied aragonite crystals is not consistent with this source.

592   The bio-mediated origin of aragonite is further supported by:

593   1- The bright auto fluorescence (Fig. 6E) of the aragonite laminae, reflecting high contents of

594   organic matter, possibly associated with autotrophic activity during intense bloom episodes.

595   2- The longitudinal cracks within the aragonite laminae, which may result from degradation of

596   EPS, acting as a template for aragonite nucleation (Obst et al., 2009).

597   We thus suggest that precipitation of aragonite in the PLG unit was biologically-mediated by

598   unknown phototrophs organisms. Possible candidates are not-fossilizing cyanobacteria or siliceous

599   algae. The concomitant presence of aragonite precipitated in the upper water column and small size

600   pyrite, indicative of euxinic condition in the lower water column (Bond and Wignall, 2010;

601   Tagliavento et al., 2020), suggests the vertical separation of the water column by an oxycline (Fig.

602   10).

603

604
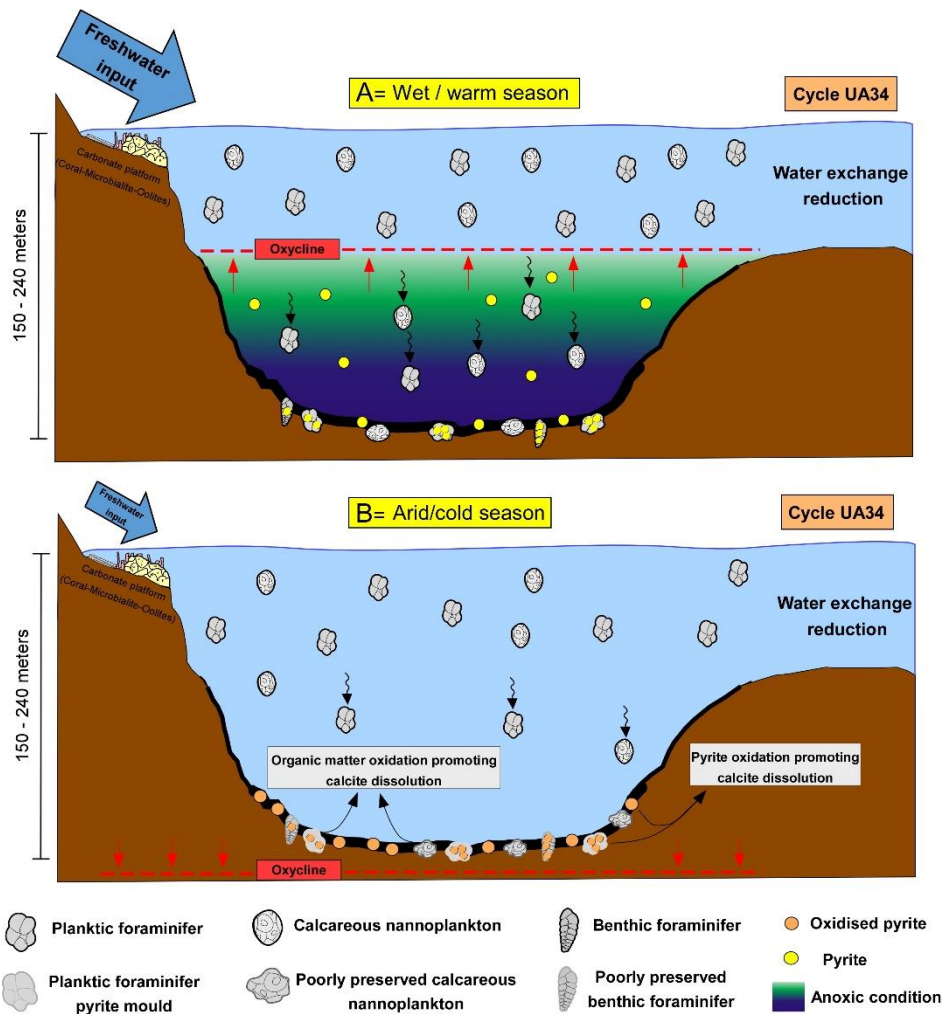
Fig. 9: Sketches showing the mechanisms promoting dissolution of calcareous fossils. A: During the wet/warm season, enhanced freshwater
input caused density stratification of the water mass. Sinking organic matter and its consequent remineralisation promoted sea bottom anoxia
and the establishment of an oxycline separating oxygenated surface water and anoxic/euxinic bottom water. Below the oxycline, pyrite
precipitated and sunk to the bottom. Pyrite was also formed inside foraminifer shells. B: During the arid/cold season, sea water cooling and
reduced freshwater input caused the vigorous mixing of the water column, with consequent migration of the oxycline below the seafloor.
This mechanism promoted the oxidation of both organic matter and pyrite, which ultimately triggered the dissolution of the biogenic calcite.

5.4 The micro and nannofossil assemblage in the PLG unit and its paleoenvironmental meaning

Calcareous micro and nannofossils re-appear in the washing residues and smear slides from cycle PLG3 upward (5.93 Ma) where they are discontinuously present, showing variable preservation (Fig. 3 and Fig. 5; supplementary material Fig. 8). Overall, little paleoenvironmental information can be obtained by the micro and nannofossil assemblage recorded in the PLG unit, because the composition of the assemblage is controlled by preservation. However, the presence of intact coccospheres and the low abundance of reworked CN in these cycles (Fig. 3) is an indication that, where preserved, the calcareous microfossil assemblages are synsedimentary and not reworked.

The appearance of shallow water ostracods (i.e. *Cyprideis*) from cycle PLG4 upwards indicates an overall shallowing of the basin with respect to the pre-MSC cycles. In the middle part of the marly hemicycle of cycle PLG6, *F. fusiformis* specimens are common, though often fragmented.

623   *Fursenkoina fusiformis* is an opportunistic shallow infaunal species (inner shelf zone) associated to

624   high organic carbon input to the sea floor, even though it can be sensitive to oxygen depletion

625   (Barmawidjaja et al., 1992; Alve and Murray, 1994). In the Northern Indian Ocean, high percentages

626   of this genus are associated to the shallow portion (50-60 m) of the Oxygen Minimum Zone

627   (Mazumder and Nigam, 2014) and it was also found at less than 40 m in the North Adriatic Sea in

628   front of the Po delta (Barmawidjaja et al. 1992). Among its ecological preferences, it is worth noting

629   the ability to rapidly recolonise the shelf after anoxic events (Alve and Murray, 1994).

630   Upward in the section, in cycle PLG7, BF are less frequent and often mostly present in the < 125

631   μm (Fig. 3). The assemblage composition (bolivinids, buliminids, uvigerinids and *Globobulimina*)

632   also suggests high organic carbon rain to the sea floor. The shallowing upward trend is further

633   confirmed by the rather common occurrence of miliolids (*Quinqueloculina* sp.) in the marly

634   hemicycle of cycle PLG9 (Fig. 3). *Quinqueloculina* is an epifaunal taxon often associated with

635   hypersaline lagoons, marine marshes or inner shelf settings (Murray, 2006); together with the

636   presence of *Cyprideis* species it suggests euryhaline conditions and the decline of organic matter

637   availability at the seafloor with respect to the lower PLG cycles. Previous studies indicated a

638   paleodepth spanning from 150-240 meters at the Abad/Yesares transition (Dronkert, 1976; Troelstra

639   et al., 1980; van de Poel, 1992; Riding et al., 1998; Baggley, 2000; Clauzon et al., 2015; Modestou et

640   al., 2017), and to 75-100 meters at the Yesares/Sorbas transition (Krijgsman et al., 2001; Roveri et al.,

641   2020), which is consistent with our data. However, the presence of miliolids, *Ammonia*, *Elphidium*,

642   and *Cyprideis,* suggests a shallower water body (less than 75 m), probably a lagoon characterized by

643   salinity fluctuations (see also Van de Poel, 1992).

644   Cycles PLG11 and PLG 12 are prevalently barren of microfossils, except for the uppermost

645   sample of cycle PLG11, where *Ammonia*, *Elphidium* and miliolids are present, confirming shallow

646   environmental conditions and salinity fluctuations (Murray, 2006).

647   The presence of calcareous plankton in such shallow environment has been often considered as the

648   result of reworking. However, in modern settings, calcareous nannoplankton (i.e. Coccolithophores)

649   was reported to proliferate in shallow (even less than 30 m) lagoonal environments (Sakka et al.,

650   1999; Sondi and Juračić, 2010; Dimiza et al., 2020), where it could be adapted to low salinity

651   conditions (Paasche et al., 1996). In modern settings, coccolithophores are recorded in low salinity

652   environments, where they can even massively bloom, as in the case of the Black Sea (Sea surface

653   Salinity ~ 18 ‰; Tyrrel et al., 2008; Kubryakov et al., 2021). They were recorded also in the Baltic

654   Sea (Kieler Forde, where maximum coccolithophore abundance occurred at salinity of 18 ‰; Meier et

655   al., 2014) and in the Aegean Sea (Thessaloniki bay, where coccolithophore maximum abundance is

656   reached with salinity of 17 ‰; Dimizia et al., 2020).

657   In our case, the CN assemblage consists of taxa tolerating low salinity conditions, such as *H.*

658   *carteri*, *Sphenolithus* gr. and *C. pelagicus* (Giraudeau et al., 1992; Silva et al., 2008; Auer et al., 2014;

659 Mancini et al., 2020), especially in cycles PLG6, PLG7 and PLG11 (Fig. 3). The scarce occurrence of

660 PF in the PLG unit could be related to the reduced water depth in respect to the pre-evaporitic phase,

661 because PF often require > 75 m water column (Schiebel and Hemleben, 2017). Furthermore, the low

662 salinity condition characterizing surface waters during the marly PLG hemicycle deposition could

663 have prevented the proliferation of PF, similarly to what observed in the modern Black Sea, where

664 living PF were never reported (Aksu et al., 2002; Gavrilova and Dolan, 2007; Wylezich and Jürgens,

665 2011). Therefore, the scattered occurrence of open marine PF (i.e *T. quinqueloba* and

666 *Globigerinoides*; Fig. 3) could suggest episodic improvement of the connection with the open sea

667 (Fig. 11).

668   The shallowing of the Sorbas Basin from cycle PLG 3 (5.93 Ma) led to salinity fluctuations in a

669 restricted environment influenced by freshwater inflows and evaporation. Runoff could have led to

670 the formation of a pycnocline; however, anoxic bottom conditions were only occasionally established,

671 as denoted by the scattered presence of pyrite and organic matter.

672

673
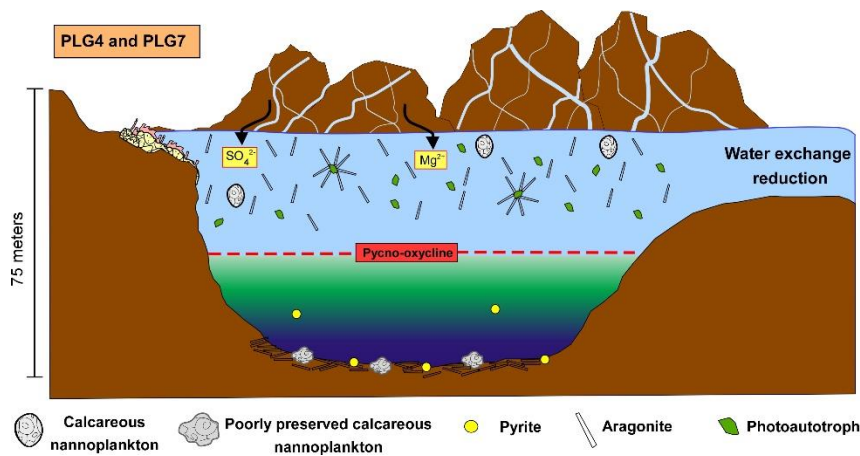
674 Fig. 10: Sketch showing the inferred mechanisms that promoted aragonite deposition and concomitant dissolution of biogenic calcite in the
675 PLG unit. Ongoing basin restriction resulted in an increased concentration of river-delivered Mg^{2+} and SO_4^{2-} ions, favouring precipitation of
676 bio-mediated aragonite and dissolution of biogenic calcite.
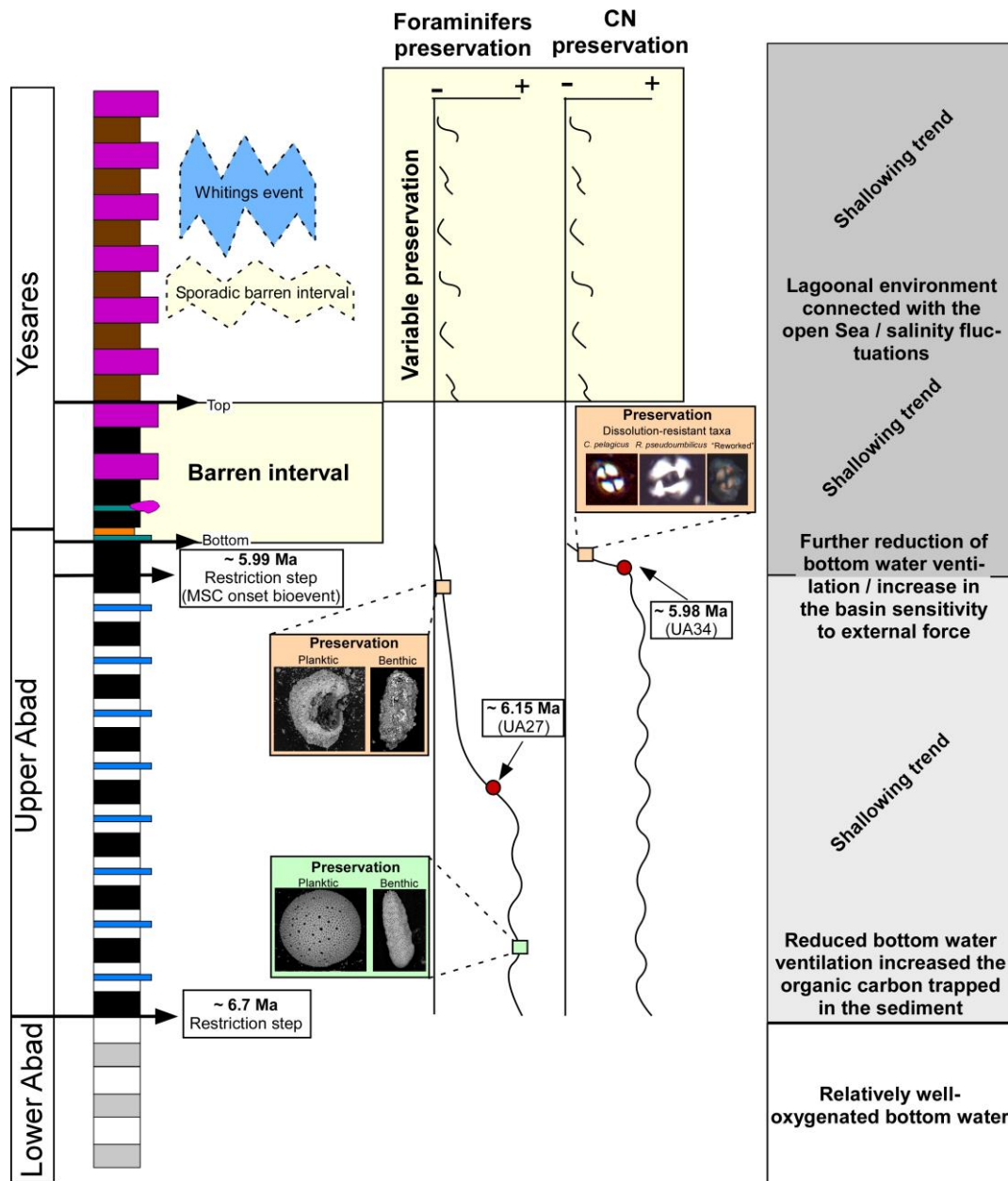
677

Fig. 11: The paleoenvironmental evolution of the Sorbas Basin toward the onset and during the MSC, with the main taphonomic

features characterizing the micro and nannofossil assemblage. The number and the thickness of the lithological cycles are schematic. Red

dots indicate the beginning of the deterioration in the preservation of calcareous micro and nannofossils. Green square indicates relatively

good preservation; orange squares indicate relatively bad preservation.

Conclusion

The micropaleontological, mineralogical, sedimentological and isotopic characterization of the

sediments spanning the onset and the first phase of MSC from the Sorbas Basin suggests that

paleoenvironmental changes in the uppermost pre-evaporitic interval (i.e. cycle UA34) led to

688 dissolution of biogenic calcite. In this interval, no evidence of increased salinity was found; rather the

689 high content of *S. abies* and *H. carteri* that characterizes the MSC onset bioevent suggests the

690 freshening of the upper water column. Calcite dissolution and the consequent disappearance of

691 calcareous micro and nannofossils approaching the MSC onset was triggered by pyrite and organic

692 matter oxidation, following climate-induced fluctuations of the redox conditions in the bottom waters

693 of a restricted basin. The calcitic fossils reappeared from 5.93 Ma onward (cycle PLG3), but the

694 assemblages are usually poorly preserved and quantitatively scarce; this fossil content is mostly

695 synsedimentary (i.e. not reworked) and still indicates restricted conditions, but in a progressively

696 shallower basin, less prone to fluctuations of redox conditions in the bottom water. The precipitation

697 of aragonite, in cycles PLG4 and PLG7, was likely bio-mediated through bloom of not-fossilising

698 autotroph organisms. Aragonite stability was likely favoured by an increase in (river-delivered) Mg^{2+}

699 and SO_4^{2-} in the seawater, which was also responsible for the poor preservation of calcitic fossils. The

700 scattered occurrence and low abundance of the open marine taxa also reflects unstable conditions in a

701 confined (lagoon) environment.

702 Our results indicate that the micropaleontological record at the onset and during the first phase of the

703 MSC (PLG unit) is strongly biased by dissolution of calcitic micro and nannofossils; such taphonomic

704 bias must be considered in the paleonvironmental reconstructions of the MSC events and in the use of

705 the disappearance of calcareous microfossil as a biostratigraphic marker approximating the onset of

706 the MSC.

707 **Acknowledgment**

References

713 Aksu, A. E., Hiscott, R. N., Kaminski, M. A., Mudie, P. J., Gillespie, H., Abrajano, T., Yaşar, D.,

714 2002. Last glacial–Holocene paleoceanography of the Black Sea and Marmara Sea: stable isotopic,

715 foraminiferal and coccolith evidence. Marine Geology, 190(1-2), 119-149.

716 Alve, E., Murray, J. W., 1994. Ecology and taphonomy of benthic foraminifera in a temperate

717 mesotidal inlet. The Journal of Foraminiferal Research, 24(1), 18-27.

718 Antonarakou, A., Kontakiotis, G., Vasilatos, C., Besiou, E., Zarkogiannis, S., Drinia, H., Mortyn,

719 P.G., Tsaparas, N., Makri, P., Karakitsios, V., 2019. Evaluating the effect of marine diagenesis on

720   Late Miocene pre-evaporitic sedimentary successions of eastern Mediterranean Sea. IOP Conference
721   Series: Earth and Environmental Sciences, 221, 012051.

722   Archer, D., Maier-Reimer, E., 1994. Effect of deep-sea sedimentary calcite preservation on
723   atmospheric CO_2 concentration. Nature, 367(6460), 260-263.

724   Archer, D., 2003. Biological Fluxes in the Ocean and Atmospheric pCO_2. Treatise on
725   Geochemistry, 6, 625.

726   Auer, G., Piller, W.E., Harzhauser, M., 2014. High-resolution calcareous nannoplankton
727   palaeoecology as a proxy for small-scale environmental changes in the Early Miocene. Marine
728   Micropaleontology, 111, 53–65.

729   Baggley, K.A., 2000. The late Tortonian-early Messinian foraminiferal record of the Abad Member
730   (Turre formation), Sorbas Basin, Almeria, south-east Spain. Palaeontology, 43, 1069–1111.

731   Barmawidjaja, D. M., Jorissen, F. J., Puskaric, S. V., Van der Zwaan, G. J., 1992. Microhabitat
732   selection by benthic foraminifera in the northern Adriatic Sea. The Journal of Foraminiferal Research,
733   22(4), 297-317.

734   Blanc-Valleron, M.M., Pierre, C., Caulet, J.P., Caruso, A., Rouchy, J.M., Cespuglio, G., Sprovieri, R.,
735   Pestrea, S., Di Stefano, E., 2002. Sedimentary, stable isotope and micropaleontological records of
736   paleoceanographic change in the Messinian Tripoli Formation (Sicily, Italy). Palaeogeography,
737   Palaeoclimatology, Palaeoecology, 185, 255–286.

738   Bond, D. P., Wignall, P. B., 2010. Pyrite framboid study of marine Permian–Triassic boundary
739   sections: a complex anoxic event and its relationship to contemporaneous mass extinction. GSA
740   Bulletin, 122(7-8), 1265-1279.

741   Bots, P., Benning, L. G., Rickaby, R., Shaw, S., 2011. The role of SO_4 in the switch from calcite to
742   aragonite seas. Geology, 39(4), 331-334.

743   Bourillot, R., Vennin, E., Rouchy, J.M., Durlet, C., Rommevaus, V., Kolodka, C., Knap, F., 2009.
744   Structure and evolution of a Messinian mixed carbonate-siliciclastic platform: the role of evaporites
745   (Sorbas Basin, South-east Spain). Sedimentology 57, 477–512.

746   Bown, P.R., Young, J.R., 1998. Techniques. In: Bown, P.R., Ed., Calcareous nannofossil
747   biostratigraphy, Chapman and Hall, London, 16-28.

748   Braga, J.C., Martin, J.M., Riding, R., Aguirre, J., Sanchez-Almazo, I.M., Dinares-Turell, J., 2006.
749   Testing models for the Messinian salinity crisis: the Messinian record in Almeria, SE Spain.
750   Sedimentary Geology, 188, 131–154.

751   Bulian, F., Kouwenhoven, T. J., Jiménez-Espejo, F. J., Krijgsman, W., Andersen, N., Sierro, F. J.,
752   2022. Impact of the Mediterranean-Atlantic connectivity and the late Miocene carbon shift on deep-

753 sea communities in the Western Alboran Basin. Palaeogeography, Palaeoclimatology, Palaeoecology,
754 110841.

755 Buckman, J., Mahoney, C., März, C., Wagner, T., 2020. The Secret 'After Life' of Foraminifera: Big
756 Things Out of Small. Minerals, 10(6), 550.

757 Burton, E.A., Walter, L.M., 1991, The effects of pCO$_2$ and temperature on magnesium incorporation
758 in calcite in seawater and MgCl$_2^-$ CaCl$_2$ solutions: Geochimica et Cosmochimica Acta, 55, 777–785.

759 Buzas-Stephens, P., Buzas, M. A., 2005. Population dynamics and dissolution of foraminifera in
760 Nueces Bay, Texas. The Journal of Foraminiferal Research, 35(3), 248-258.

761 Carnevale, G., Gennari, R., Lozar, F., Natalicchio, M., Pellegrino, L., Dela Pierre, F., 2019. Living in
762 a deep desiccated Mediterranean Sea: an overview of the Italian fossil record of the Messinian salinity
763 crisis. Bollettino della Società Paleontologica Italiana, 58, 109–140.

764 Capella, W., Barhoun, N., Flecker, R., Hilgen, F. J., Kouwenhoven, T., Matenco, L. C., Sierro, F.J.,
765 Tulbure, M.A., Yousfi, M.Z., Krijgsman, W., 2018. Palaeogeographic evolution of the late Miocene
766 Rifian Corridor (Morocco): reconstructions from surface and subsurface data. Earth-Science
767 Reviews, 180, 37-59.

768 Catalano R., Di Stefano E., Sprovieri R., Lena G., Valenti V., 2016. The barren Messinian Tripoli in
769 Sicily and its palaeoenvironmental evolution: suggestions on the exploration potential. Petroleum
770 Geosciences, 22, 322-332

771 Chiu, T. C., Broecker, W. S., 2008. Toward better paleocarbonate ion reconstructions: New insights
772 regarding the CaCO$_3$ size index. Paleoceanography, 23(2).

773 Clauzon, G., Suc, J.P., Do Couto, D., Jouannic, G., Melinte-Dobrinescu, M.C., Jolivet, L., Martinell,
774 J., 2015. New insights on the Sorbas Basin (SE Spain): the onshore reference of the Messinian salinity
775 crisis Marine and Petroleum Geology 66, 71–100.

776 Corbi, H., Lancis, C., Giannetti, A., Tent-Manclus, J.E., Dinares- Turell, J., 2016. Sedimentological
777 and paleoenvironmental scenario before, during, and after the Messinian Salinity Crisis: the San
778 Miguel de Salinas composite section (western Mediterranean). Marine Geology 379, 246–266.

779 Corbí, H., Soria, J.M., 2016. Late Miocene–early Pliocene planktonic foraminifer event-stratigraphy
780 of the Bajo Segura basin: a complete record of the western Mediterranean. Marine and Petroleum
781 Geology, 77, 1010–1027.

782 Corbí, H., Soria, J. M., Giannetti, A., Yébenes, A., 2020. The step-by-step restriction of the
783 Mediterranean (start, amplification, and consolidation phases) preceding the Messinian Salinity Crisis
784 (climax phase) in the Bajo Segura basin. Geo-Marine Letters, 40(3), 341-361.

785 Dela Pierre, F., Clari, P., Natalicchio, M., Ferrando, S., Giustetto, R., Lozar, F., Lugli, S., Manzi, V.,
786 Roveri, M., Violanti, D., 2014. Flocculent layers and bacterial mats in the mudstone interbeds of the
787 primary lower Gypsum unit (Tertiary Piedmont basin, NW Italy): archives of palaeoenvironmental
788 changes during the Messinian salinity crisis. Marine Geology, 355, 71–87.

789 Dimiza, M. D., Koukousioura, O., Michailidis, I., Dimou, V. G., Navrozidou, V., Aligizaki, K.,
790 Seferlis, M., 2020. Seasonal living coccolithophore distribution in the enclosed coastal environments
791 of the Thessaloniki Bay (Thermaikos Gulf, NW Aegean Sea). Revue de Micropaléontologie, 69,
792 100449.

793 Drinia, H., Antonarakou, A., Tsaparas, N., Kontakiotis, G., 2007. Palaeoenvironmental conditions
794 preceding the Messinian Salinity Crisis: A case study from Gavdos Island. Geobios, 40, 251-265.

795 Dronkert, H., 1976. Late Miocene evaporites in the Sorbas Basin and adjoining areas. Memorie della
796 Società Geologica Italiana, 341–361.

797 Flecker, R., Krijgsman, W., Capella, W., de Castro Martins, C., Dmitrieva, E., Mayser, J.P.,
798 Marzocchi, A., Modestou, S., Ochoa, D., Simon, D., Tulbure, M., van den Berg, B., van der Schee,
799 M., de Lange, G., Ellam, R., Govers, R., Gutjahr, M., Hilgen, F., Kouwenhoven, T., Lofi, J., Meijer,
800 P., Sierro, F.J., Bachiri, N., Barhoun, N., Alami, A.C., Chacon, B., Flores, J.A., Gregory, J., Howard,
801 J., Lunt, D., Ochoa, M., Pancost, R., Vincent, S., Yousfi, M.Z., 2015. Evolution of the Late Miocene
802 Mediterranean- Atlantic gateways and their impact on regional and global environmental change.
803 Earth Science Review, 150, 365–392.

804 Fortuin, A. R., Krijgsman, W., 2003. The Messinian of the Nijar Basin (SE Spain): sedimentation,
805 depositional environments and paleogeographic evolution. Sedimentary Geology, 160(1-3), 213-242.

806 Gavrilova, N., Dolan, J., 2007. A note on species lists and ecosystem shifts: Black Sea tintinnids,
807 ciliates of the microzooplankton. Acta Protozoologica, 46, 279-288.

808 Gennari, R., Manzi, V., Angeletti, L., Bertini, A., Biffi, U., Ceregato, A., Faranda, C., Gliozzi, E.,
809 Lugli, S., Menichetti, E., Rosso, A., Roveri, M., Taviani, M., 2013. A shallow water record of the
810 onset of the Messinian salinity crisis in the Adriatic foredeep (Legnagnone section, Northern
811 Apennines). Palaeogeography, Palaeoclimatology, Palaeoecology, 386, 145-164.

812 Gennari, R., Lozar, F., Turco, E., Dela Pierre, F., Manzi, V., Natalicchio, M., Lugli, S., Roveri, M.,
813 Schreiber, B.C., Taviani, M., 2018. Integrated stratigraphy and paleoceanographic evolution of the
814 pre-evaporitic phase of the Messinian salinity crisis in the Eastern Mediterranean as recorded in the
815 Tokhni section (Cyprus island). Newsletters on Stratigraphy, 51, 33–55.

816 Gennari, R., Lozar, F., Natalicchio M., Zanella, E., Carnevale, G., Dela Pierre, F., 2020. Chronology
817 of the Messinian events in the northernmost part of the Mediterranean: the Govone section (Piedmont
818 Basin, NW Italy). Rivista Italiana di Paleontologia e Stratigrafia, 126, 517–60.

819   Gibbs, S., Shackleton, N., Young, J.R., 2004. Orbitally forced climate signals in mid- Pliocene

820   nannofossil assemblages. Marine Micropaleontology, 51, 39–56.

821   Giraudeau, J., 1992. Distribution of recent nannofossils beneath the Benguela system: southwest

822   African continental margin. Marine Geology 108, 219–237.

823   Goubert, E., Néraudeau, D., Rouchy, J. M., Lacour, D., 2001. Foraminiferal record of environmental

824   changes: Messinian of the Los Yesos area (Sorbas Basin, SE Spain). Palaeogeography,

825   Palaeoclimatology, Palaeoecology, 175(1-4), 61-78.

826   Hsü, K.J., Montadert, L., Bernoulli, D., Cita, M.B., Erikson, A., Garrison, R.E., Kidd, R.B., Mélières,

827   F., Muller, C., Wright, R.H., 1977. History of the Mediterranean salinity crisis. Nature, 267(5610),

828   399-403.

829   Jahnke, R. A., Craven, D. B., McCorkle, D. C., Reimers, C. E., 1997. $CaCO_3$ dissolution in California

830   continental margin sediments: The influence of organic matter remineralization. Geochimica et

831   Cosmochimica Acta, 61(17), 3587-3604.

832   Karakitsios, V., Roveri, M., Lugli, S., Manzi, V., Gennari, G., Antonarakou, A., Triantaphyllou, M.,

833   Agiadi, K., Kontakiotis, G., Kafousia, N., de Rafelis, M., 2017. A record of the Messinian salinity

834   crisis in the eastern Ionian tectonically active domain (Greece, eastern Mediterranean). Basin

835   Research 29, 203–233.

836   Kontakiotis, G., Besiou, E., Antonarakou, A., Zarkogiannis, S., Kostis, A., Mortyn, P.G., Moissette,

837   P., Cornée, J.J., Schulbert, C., Drinia, H., Anastasakis, G., Karakitsios,V., 2019. Decoding sea surface

838   and paleoclimate conditions in the eastern Mediterranean over the Tortonian-Messinian Transition.

839   Palaeogeography, Palaeoclimatology, Palaeoecology, 534, 109312.

840   Kontakiotis, G., Karakitsios, V., Cornée, J., Moissette, P., Zarkogiannis, S.D., Pasadakis, N.,

841   Koskeridou, E., Manoutsoglou, E., Drinia, H., Antonarakou, A., 2020. Preliminary results based on

842   geochemical sedimentary constraints on the hydrocarbon potential and depositional environment of a

843   Messinian sub-salt mixed siliciclastic-carbonate succession onshore Crete (Plouti section, eastern

844   Mediterranean). Mediterranean Geoscience Review, 2, 247-265.

845   Kontakiotis, G., Karakitsios, V., Maravelis, A.G, Zarkogiannis, S.D., Agiadi, K., Antonarakou, A.,

846   Pasadakis, N., Zelilidis, A., 2021. Integrated isotopic and organic geochemical constraints on the

847   depositional controls and source rock quality of the Neogene Kalamaki sedimentary successions

848   (Zakynthos Island, Ionian Sea). Mediterranean Geoscience Review, 3,193–217.

849   Kontakiotis, G., Butiseacă, G. A., Antonarakou, A., Agiadi, K., Zarkogiannis, S. D., Krsnik, E.,

850   Besiou, E., Zachariasse, W.J., Lourens, L., Thivaiou, D., Kosteridou, E., Moisette, P., Mulch, A.,

851   Karakitsios, V., Vasiliev, I., 2022. Hypersalinity accompanies tectonic restriction in the eastern

852   Mediterranean prior to the Messinian Salinity Crisis. Palaeogeography, Palaeoclimatology,
853   Palaeoecology, 592, 110903.

854   Kouwenhoven, T.J., Seidenkrantz, M.S., van der Zwaan, G.J., 1999. Deep-water changes: the near
855   synchronous disappearance of a group of benthic foraminifera from the Late Miocene Mediterranean.
856   Palaeogeography, Palaeoclimatology, Palaeoecology. 152, 259–281.

857   Kouwenhoven, T.J., Morigi, C., Negri, A., Giunta, S., Krijgsman, W., Rouchy, J.M., 2006.
858   Palaeoenvironmental evolution of the eastern Mediterranean during the Messinian: constraints from
859   integrated microfossil data of the Pissouri Basin (Cyprus). Marine Micropaleontology, 60, 17–44.

860

861   Krijgsman, W., Hilgen, F. J., Raffi, I., Sierro, F. J., Wilson, D. S., 1999. Chronology, causes and
862   progression of the Messinian salinity crisis. Nature, 400(6745), 652-655.

863   Krijgsman, W., Fortuin, A. R., Hilgen, F. J., Sierro, F. J., 2001. Astrochronology for the Messinian
864   Sorbas basin (SE Spain) and orbital (precessional) forcing for evaporite cyclicity. Sedimentary
865   Geology, 140(1-2), 43-60.

866   Krijgsman, W., Leewis, M. E., Garcés, M., Kouwenhoven, T. J., Kuiper, K. F., Sierro, F. J., 2006.
867   Tectonic control for evaporite formation in the Eastern Betics (Tortonian; Spain). Sedimentary
868   Geology, 188, 155-170.

869   Kubryakov, A. A., Mikaelyan, A. S., Stanichny, S. V., 2021. Extremely strong coccolithophore
870   blooms in the Black Sea: The decisive role of winter vertical entrainment of deep water. Deep Sea
871   Research Part I: Oceanographic Research Papers, 173, 103554.

872   Lacour, D., Nèraudeau, D., 2000. Évolution de la diversité des *Brissopsis* intragypses de Sorbas (SE
873   Espagne). Geodiversitas, 22(4), 509-523.

874   Landini W., Sorbini L., 1989. Ichthyofauna of the evaporitic Messinian in the Romagna and Marche
875   regions. Bollettino della Società Paleontologica Italiana, 28, 287-293.

876   Larson, E. B., Mylroie, J. E., 2014. A review of whiting formation in the Bahamas and new
877   models. Carbonates and Evaporites, 29(4), 337-347.

878   Lee, D., Carpenter, S. J., 2001. Isotopic disequilibrium in marine calcareous algae. Chemical
879   geology, 172(3-4), 307-329.

880   Lirer, F., Foresi, L. M., Iaccarino, S. M., Salvatorini, G., Turco, E., Cosentino, C., Sierro, F.J., Caruso,
881   A., 2019. Mediterranean Neogene planktonic foraminifer biozonation and biochronology. Earth-
882   Science Reviews, 196, 102869.

883   Liu, X., Li, A., Dong, J., Zhuang, G., Xu, F., Wan, S., 2018. Nonevaporative origin for gypsum in
884   mud sediments from the East China Sea shelf. Marine Chemistry, 205, 90-97.

885   Loreau, J.P., 1982, Sediments aragonitiques et leur denise: Memoires du Museum National d'Histoire
886   Naturelle, Serie C., Tome XLVI1, 300 p.

887   Lozar, F., Violanti, D., Bernardi, E., Dela Pierre, F., Natalicchio, M., 2018. Identifying the onset of
888   the Messinian salinity crisis: a reassessment of the biochronostratigraphic tools (Piedmont Basin, NW
889   Italy). Newsletter on Stratigraphy 51(1), 11–31.

890   Lozar, F., Negri, A., 2019. A review of basin-wide calcareous nannofossil bioevents in the
891   Mediterranean at the onset of the Messinian salinity crisis. Marine Micropaleontology 151, 101752.

892   Lugli, S., Manzi, V., Roveri, M., Schreiber, B. C., 2010. The Primary Lower Gypsum in the
893   Mediterranean: a new facies interpretation for the first stage of the Messinian salinity crisis.
894   Palaeogeography, Palaeoclimatology, Palaeoecology, 297, 83–99.

895   Macintyre I. G., Reid R.P., 1992. Comment on the origin of aragonite needle mud: a picture is worth a
896   thousand words. Journal of Sedimentary Petrology 62,1095–1097.

897   Macintyre, I. G., Reid, R. P., 1995. Crystal alteration in a living calcareous alga (*Halimeda*);
898   implications for studies in skeletal diagenesis. Journal of Sedimentary Research, 65(1a), 143-153.

899   Mancini, A. M., Gennari, R., Ziveri, P., Mortyn, P. G., Stolwijk, D. J. Lozar, F., 2020. Calcareous
900   nannofossil and foraminiferal trace element records in the Sorbas Basin: A new piece of the
901   Messinian Salinity Crisis onset puzzle. Palaeogeography, Palaeoclimatology, Palaeoecology, 554,
902   109796.

903   Mancini, A. M., Grelaud, M., Ziveri, P., Nallino, E., Lozar, F., 2021. Calcareous nannofossil size and
904   abundance response to the Messinian Salinity Crisis onset and paleoenvironmental
905   dynamics. Paleoceanography and Paleoclimatology, 36(9), e2020PA004155.

906   Manzi, V., Roveri, M., Gennari, R., Bertini, A., Biffi, U., Giunta, S., Iaccarino, S.M., Lanci, L., Lugli,
907   S., Negri, A., Riva, A., Rossi, M.E., Taviani, M., 2007. The deep-water counterpart of the Messinian
908   Lower Evaporites in the Apennine foredeep: the Fanantello section (Northern Apennines, Italy).
909   Palaeogeography, Palaeoclimatology, Palaeoecology. 251, 470–499.

910   Manzi, V., Gennari, R., Hilgen, F., Krijgsman, W., Lugli, S., Roveri, M., Sierro, F.J., 2013. Age
911   refinement of the Messinian salinity crisis onset in the Mediterranean. Terra Nova 25, 315–322.

912   Manzi, V., Gennari, R., Lugli, S., Minelli, N., Reghizzi, M., Roveri, M., Schreiber, B. C., 2016.
913   Comment on "Carbonate deposition and diagenesis in evaporitic environments: The evaporative and
914   sulphur-bearing limestones during the settlement of the Messinian Salinity Crisis in Sicily and
915   Calabria" by Caruso et al., 2015. Palaeo3, 429, 136–162. Palaeogeography, Palaeoclimatology,
916   Palaeoecology, 459, 585-596.

917   Manzi, V., Gennari, R., Lugli, S., Persico, D., Reghizzi, M., Roveri, M., Schreiber, B. C., Calvo, R.,

918   Gavrieli, I., Gvirtzman, Z., 2018. The onset of the Messinian salinity crisis in the deep Eastern

919   Mediterranean basin. Terra Nova, 30(3), 189-198.

920   Mayser, J. P., Flecker, R., Marzocchi, A., Kouwenhoven, T. J., Lunt, D. J., Pancost, R. D., 2017.

921   Precession driven changes in terrestrial organic matter input to the Eastern Mediterranean leading up

922   to the Messinian Salinity Crisis. Earth and Planetary Science Letters, 462, 199-211.

923   Mazumder, A., Nigam, R., 2014. Bathymetric preference of four major genera of rectilinear benthic

924   foraminifera within oxygen minimum zone in Arabian Sea off central west coast of India. Journal of

925   Earth System Science, 123(3), 633-639.

926   McNeil, D. H., 1997. Diagenetic regimes and the foraminiferal record in the Beaufort-Mackenzie

927   Basin and adjacent cratonic areas. Annales Societatis Geologorum Poloniae, 67(2-3), 271-286.

928   Meier, K. S., Kinkel, H., Young, J., 2014. A note on calcareous nannoplankton from the Kieler Förde

929   (Baltic Sea). Journal of Nannoplankton Research, 33, 29-37.

930   Milliman, J. D., 1974. Precipitation and cementation of deep-sea carbonate sediments. Deep-Sea

931   Sediments (463-476). Springer, Boston, MA.

932   Milliman, J.D., Freile, D., Steinen, R.P. Wilber, R.J., 1993. Great Bahama Bank aragonitic muds:

933   mostly inorganically precipitated, mostly exported. Journal of Sedimentary Petrology, 63, 589–595.

934   Modestou, S., Simon, D., Gutjahr, M., Marzocchi, A., Kowenhoven, T.J., Ellam, R.M., Flecker, R.,

935   2017. Precessional variability of 87Sr/86Sr in the late Miocene Sorbas Basin: an interdisciplinary

936   study of drivers of interbasin exchange. Paleoceanography, 32, 1–22.

937   Moissette, P., Cornée, J.- J., Antonarakou, A., Kontakiotis, G., Drinia, H., Koskeridou, E., Tsourou,

938   T., Agiadi, K., Karakitsios, V., 2018. Palaeoenvironmental changes at the Tortonian/Messinian

939   boundary: A deep-sea sedimentary record of the eastern Mediterranean Sea. Palaeogeography,

940   Palaeoclimatology, Palaeoecology, 505, 217-233.

941   Montenat, C., Ott d'Estevou, P., Plaziat, J. C., Chapel, J., 1980. La signification des faunes marines

942   contemporaines des évaporites messiniennes dans le Sud-Est de l'Espagne. Conséquences pour

943   l'interprétation des conditions d'isolement de la Méditerranée occidentale. Géologie

944   méditerranéenne, 7(1), 81-89.

945   Morse, J. W., Wang, Q., Tsio, M. Y., 1997. Influences of temperature and Mg:Ca ratio on $CaCO_3$

946   precipitates from seawater. Geology, 25(1), 85-87.

947   Murray, J. W., 2006. Ecology and applications of benthic foraminifera. Cambridge University Press.

948   Natalicchio, M., Dela, Pierre F., Birgel, D., Brumsack, H., Carnevale, G., Gennari, R., Gier, S., Lozar,

949   F., Pellegrino, L., Sabino, M., Schnetger, B., Peckmann, J., 2019. Paleoenvironmental change in a

950 precession-paced succession across the onset of the Messinian salinity crisis: Insight from element

951 geochemistry and molecular fossils. Palaeogeography, Palaeoclimatology, Palaeoecology, 518, 45–

952 61.

953 Néraudeau D., Videt B., Courville P., Goubert E., Rouchy J.-M., 2002. Corrélation des niveaux

954 fossilifères marins interstratifés dans les gypses messiniens, entre la carrière de Molinos de Aguas

955 (bassin de Sorbas, SE Espagne). Geodiversitas, 24, 659-667.

956 Obst, M., Dynes, J., Lawrence, J., Swerhone, G., Benzerara, K., Karunakaran, C., Kaznatcheev K.,

957 Tyliszczak, T., Hitchcock A.P., 2009. Precipitation of amorphous $CaCO_3$ (aragonite-like) by

958 cyanobac-teria: a STXM study of the influence of EPS on the nucleation process. Geochimica

959 Cosmochimica Acta, 73, 4180–4198.

960 Paasche, E., Brubak, S., Skattebøl, S., Young, J. R., Green, J. C. 1996. Growth and calcification in the

961 coccolithophorid Emiliania huxleyi (Haptophyceae) at low salinities. Phycologia, 35(5), 394-403.

962 Pellegrino, L., Natalicchio, M., Abe, K., Jordan, R. W., Longo, S. E. F., Ferrando, S., Carnevale, G.,

963 Dela Pierre, F., 2021. Tiny, glassy, and rapidly trapped: The nano-sized planktic diatoms in Messinian

964 (late Miocene) gypsum. Geology, 49(11), 1369-1374.

965 Perri, E., Gindre-Chanu, L., Caruso, A., Cefalà, M., Scopelliti, G., Tucker, M., 2017. Microbial-

966 mediated pre-salt carbonate deposition during the Messinian salinity crisis (Calcare di Base fm.,

967 Southern Italy). Marine and Petroleum Geology, 88, 235-250.

968 Peterson, L. C., Prell, W. L., 1985. Carbonate dissolution in recent sediments of the eastern equatorial

969 Indian Ocean: preservation patterns and carbonate loss above the lysocline. Marine Geology, 64(3-4),

970 259-290.

971 Pierre, C., 1999. The oxygen and carbon isotope distribution in the Mediterranean water

972 masses. Marine geology, 153(1-4), 41-55.

973 Pierre, C., Rouchy, J. M., 2004. Isotopic compositions of diagenetic dolomites in the Tortonian marls

974 of the western Mediterranean margins: evidence of past gas hydrate formation and dissociation.

975 Chemical Geology, 205(3-4), 469-484.

976 Reghizzi, M., Gennari, R., Douville, E., Lugli, S., Manzi, V., Montagna, P., Roveri, M., Sierro, F.J.,

977 Taviani, M., 2017. Isotope stratigraphy (87Sr/86Sr, δ18O, δ13C) of the Sorbas basin (Betic

978 Cordillera, Spain): Paleoceanographic evolution across the onset of the Messinian salinity crisis.

979 Palaeogeography, Palaeoclimatology, Palaeoecology, 469, 60–73.

Riding, R., Braga, J.C., Martin, J.M., Sanchez-Almazo, I.M., 1998. Mediterranean Messinian salinity crisis: constraints from a coeval marginal basin, Sorbas, southeastern Spain. Marine Geology, 146, 1–20.

Robbins, L.L., Blackwelder, P.L., 1992. Biochemical and ultrastructural evidence for the origin of whitings: a biologically induced calcium carbonate precipitation mechanism. Geology 20, 464–468.

Roep, T. B., Dabrio, C. J., Fortuin, A. R., Polo, M. D., 1998. Late highstand patterns of shifting and stepping coastal barriers and washover-fans (late Messinian, Sorbas Basin, SE Spain). Sedimentary Geology, 116, 27–56.

Roth, P. H., Berger, W. H., 1975. Distribution and dissolution of coccoliths in the South and central Pacific, Foraminiferal Research, 13, 87–113.

Roth, P. H., Coulbourn, W. T., 1982. Floral and solution patterns of coccoliths in surface sediments of the North Pacific, Marine Micropaleontology, 7, 1– 52.

Rouchy, J. M., Caruso, A., 2006. The Messinian salinity crisis in the Mediterranean basin: a reassessment of the data and an integrated scenario. Sedimentary Geology, 188, 35-67.

Roveri, M., Gennari, R., Lugli, S., Manzi, V., 2009. The Terminal Carbonate Complex: the record of sea-level changes during the Messinian salinity crisis. GeoActa 8, 57–71.

Roveri, M., Flecker, R., Krijgsman, W., Lofi, J., Lugli, S., Manzi, V., Sierro, F.J., Bertini, A., Camerlenghi, A., De Lange, G., Govers, R., Hilgen, F.J., Hubscher, C., Meijer, P.T., Stoica, M., 2014. The Messinian Salinity Crisis: past and future of a great challenge for marine sciences. Marine Geology, 352, 25–58.

Roveri, M., Gennari, R., Persico, D., Rossi, F. P., Lugli, S., Manzi, V., Reghizzi, M., Taviani, M., 2019. A new chronostratigraphic and palaeoenvironmental framework for the end of the Messinian salinity crisis in the Sorbas Basin (Betic Cordillera, southern Spain). Geological Journal, 54(3), 1617-1637.

Roveri, M., Lugli, S., Manzi, V., Reghizzi, M., Rossi, F. P., 2020. Stratigraphic relationships between shallow-water carbonates and primary gypsum: insights from the Messinian succession of the Sorbas Basin (Betic Cordillera, Southern Spain). Sedimentary Geology, 404, 105678.

Ruegg, G. J. H., 1964. Geologische onderzoekingen in het bekken van Sorbas, S Spanje. Amsterdam Geological Institut, University of Amsterdam, 64.

Sabino, M., Schefuß, E., Natalicchio, M., Dela Pierre, F., Birgel, D., Bortels, D., Schnetger, B., Peckmann, J., 2020. Climatic and hydrologic variability in the northern Mediterranean across the onset of the Messinian salinity crisis. Palaeogeography, Palaeoclimatology, Palaeoecology, 545, 109632.

1013 Saint Martin, J. P., Pestrea, S., Conesa, G., 2001. Les assemblages de diatomées des niveaux infra-
1014 gypseux du bassin messinien de Sorbas (Espagne). Cryptogamie Algologie, 22(1), 127-149.

1015 Sakka, A., Legendre, L., Gosselin, M., LeBlanc, B., Delesalle, B., Price, N. M., 1999. Nitrate,
1016 phosphate, and iron limitation of the phytoplankton assemblage in the lagoon of Takapoto Atoll
1017 (Tuamotu Archipelago, French Polynesia). Aquatic Microbial Ecology, 19(2), 149-161.

1018 Schiebel, R., Hemleben, C., 2017. Planktic foraminifers in the modern ocean. Berlin, Springer, 1-358.

1019 Shinn, E.A., Steinen, R.P., Lidz, B.H. Swart, P.K., 1989. Whitings, a sedimentologic dilemma.
1020 Journal of Sedimentary Petrology, 59, 147– 161.

1021 Sierro, F.J., Hilgen, F.J., Krijgsman, W., Flores, J.A., 2001. The Abad composite (SE Spain): a
1022 Mediterranean and global reference section for the Messinian. Palaeogeography, Palaeoclimatology,
1023 Palaeoecology, 168, 141–169.

1024 Sierro, F.J., Flores, J.A., Bàrcena, M.A., Vazquez, A., Utrilla, R., Zamarreno, I., 2003. Orbitally-
1025 controlled oscillations in the planktic communities and cyclical changes in western Mediterranean
1026 hydrography during the Messinian. Palaeogeography, Palaeoclimatology, Palaeoecology, 190, 289–
1027 316

1028 Silva, A., Palma, S., Moita, M.T., 2008. Coccolithophores in the upwelling waters of Portugal: four
1029 years of weekly distribution in Lisbon bay. Continental Shelf Research, 28, 2601–2613.

1030 Sondi, I., Juračić, M., 2010. Whiting events and the formation of aragonite in Mediterranean Karstic
1031 Marine Lakes: new evidence on its biologically induced inorganic origin. Sedimentology, 57(1), 85-
1032 95.

1033 Sprovieri, R., Di Stefano, E., Sprovieri, M., 1996. High resolution chronology for Late Miocene
1034 Mediterranean stratigraphic events. Rivista Italiana di Paleontologia e Stratigrafia, 102, 77–104.

1035 Steinsund, P. I., Hald, M., 1994. Recent calcium carbonate dissolution in the Barents Sea:
1036 Paleoceanographic applications. Marine Geology, 117(1-4), 303-316.

1037 Suárez-Ibarra, J. Y., Frozza, C. F., Palhano, P. L., Petró, S. M., Weinkauf, M. F., Pivel, M. A., 2022.
1038 Calcium carbonate dissolution triggered by high productivity during the last glacial-interglacial
1039 interval at the deep western South Atlantic. Frontiers in Earth Science, 10, 830984.

1040 Subhas, A. V., Rollins, N. E., Berelson, W. M., Erez, J., Ziveri, P., Langer, G., Adkins, J. F., 2018.
1041 The dissolution behavior of biogenic calcites in seawater and a possible role for magnesium and
1042 organic carbon. Marine Chemistry, 205, 100-112.

1043 Swart, P. K., 1983. Carbon and oxygen isotope fractionation in scleractinian corals: a review. Earth-
1044 science reviews, 19(1), 51-80.

1045 Swart, P.K. Eberli, G.P., 2005. The nature of the δ ^{13}C of periplatform sediments: implications for
1046 stratigraphy and the global carbon cycle. Sedimentary Geology, 175, 115–130.

1047 Swart, P.K., Reijmer, J.J. Otto, R., 2009. A re evaluation of facies on Great Bahama Bank II:
1048 variations in the δ^{13}C, δ ^{18}O and mineralogy of surface sediments. In: Perspectives in Carbonate
1049 Geology: A Tribute to the Career of Robert Nathan Ginsburg, IAS Special Publication (Eds P.K.
1050 Swart, G.P. Eberli and J.A. McKenzie), 41, 47–60. Wiley- Blackwell, Oxford

1051 Tagliavento M., Lauridsen, B. W., Stemmerik, L., 2020. Episodic dysoxia during Late Cretaceous
1052 cyclic chalk-marl deposition – Evidence from framboidal pyrite distribution in the upper
1053 Maastrichtian Rørdal Mb., Danish Basin. Cretaceous Research 106, 104223.

1054 Trenkwalder S., Violanti D., d'Atri A., Lozar F., Dela Pierre F., Irace A., 2008. The
1055 Miocene/Pliocene boundary and the Early Pliocene micropaleontological record: new data from the
1056 Tertiary Piedmont Basin (Moncucco quarry, Turin Hill, Northwestern Italy). Bollettino della Società
1057 Paleontologica Italiana, 47 (2), 87-103.

1058 Troelstra, S.R., Van der Poel, H.M., Huisman, C.H.A., Geerlings, L.P.A., Dronkert, H., 1980.
1059 Paleoecological changes in the latest Miocene of the Sorbas Basin, S.E. Spain. Geologie
1060 Méditerranéenne. 8, 115–126.

1061 Turpin, M., Emmanuel, L., Reijmer, J. J., Renard, M. 2011. Whiting-related sediment export along the
1062 Middle Miocene carbonate ramp of Great Bahama Bank. International Journal of Earth
1063 Sciences, 100(8), 1875-1893.

1064 Tyrrell, T., Schneider, B., Charalampopoulou, A., Riebesell, U., 2008. Coccolithophores and calcite
1065 saturation state in the Baltic and Black Seas. Biogeosciences, 5(2), 485-494.

1066 van de Poel, H. M., 1992. Foraminiferal biostratigraphy and palaeoenvironments of the Miocene-
1067 Pliocene Carboneras-Nijar basin (SE Spain). Scripta Geologica, 102, 1-32.

1068 Vasiliev, I., Karakitsios, V., Bouloubassi, I., Agiadi, K., Kontakiotis, G., Antonarakou, A.,
1069 Triantaphyllou, M., Gogou, A., Kafousia, N., de Rafélis, M., Zarkogiannis, S., Kaczmar, F., Parinos,
1070 C., Pasadakis, N., 2019. Large sea surface temperature, salinity, and productivity-preservation
1071 changes preceding the onset of the Messinian Salinity Crisis in the eastern Mediterranean Sea.
1072 Paleoceanography and Paleoclimatology, 34(2), 182-202.

1073 Violanti D., Lozar F., Dela Pierre F., Natalicchio M., Bernardi E., Clari P. Cavagna S., 2013. Stress-
1074 tolerant microfossils of a Messinian succession from the Northern Mediterranean basin (Pollenzo
1075 section, Piedmont, northwestern Italy). Bollettino della Società Paleontologica Italiana, 52, 45-54.

1076 Volk, H.R., Rondeel, H.E., 1967. Zur gliederung des Jungtertiärs in becken von Vera, Südost Spanien.
1077 Geologie en Mijnbouw 43, 310-315.

1078   Weber, J. N., Raup, D. M., 1966. Fractionation of the stable isotopes of carbon and oxygen in marine

1079   calcareous organisms—the Echinoidea. Part I. Variation of ^{13}C and ^{18}O content within

1080   individuals. Geochimica et Cosmochimica Acta, 30(7), 681-703.

1081   Wylezich, C., Jürgens, K., 2011. Protist diversity in suboxic and sulfidic waters of the Black

1082   Sea. Environmental microbiology, 13(11), 2939-2956.

1083   Yates K. K., Robbins, L. L., 1998. Production of carbonate sediments by unicellular green alga.

1084   American Mineralogist, 83,1503–1509.

1085   Zachariasse, W. J., Kontakiotis, G., Lourens, L. J., Antonarakou, A., 2021. The Messinian of Agios

1086   Myron (Crete, Greece): A key to better understanding diatomite formation south of Crete, on Gavdos

1087   Island. Palaeogeography, Palaeoclimatology, Palaeoecology, 581, 110633.

1088   Ziegenbalg, S.B., Brunner, B., Rouchy, J.M., Birgel, D., Pierre, C., Böttcher, M.E., Caruso, A.,

1089   Immenhauser, A., Peckmann, J., 2010. Formation of secondary carbonates and native sulphur in

1090   sulphate-rich Messinian strata, Sicily. Sedimentary Geology, 227, 37-50.

1091